A SPECTROSCOPIC STUDY OF PULSATIONS IN γ DORADUS STARS

THOMAS ROBERT SHUTT

MSc by Research

University of York

Physics

March 2018

ABSTRACT

Two candidate γ Doradus stars are analysed: HD 103257 and HD 109799. Over 250 spectra were gathered for analysis using the HERCULES spectrograph at the University of Canterbury Mt John Observatory. The spectra for each star were cross-correlated with synthetic spectra to produce line profiles and augmented with photometric data from the WASP archive and HIPPARCOS catalogue for frequency and mode analysis.

Three pulsation frequencies were identified for HD 103257: 1.22496 ± 0.00001 d^{-1}, 1.14569 ± 0.00002 d^{-1} and 0.67308 ± 0.00004 d^{-1}, explaining 66.6% of the variation across the line profiles. The frequencies were characterised with best-fit modes of (ℓ, m) = (1, 1), (1, 1) and (3, -2) respectively. The inclination of the rotation axis and the radius were best-fit to i = 86.4° and R = 2.6 $R_{\odot}$, while a zero-point fit yielded a $v\sin i$ of 71.5 km s^{-1}.

Three pulsation frequencies were identified for HD 109799: 1.48679 ± 0.00002 d^{-1}, 1.25213 ± 0.00002 d^{-1} and 0.92184 ± 0.00004 d^{-1} , explaining 39.3% of the variation across the line profiles. The frequencies yielded individual mode fits of modes (ℓ, m) = (1, 1), (1, 1) and (3, 2). The rotational axis for HD 109799 to the range i = 65° - 70° with a zero-point fitted $v\sin i$ of 40.2 km s^{-1}.

Based on observations of frequencies and modes characteristic of the class, HD 103257 and HD 109799 can now be categorised as bona fide γ Doradus stars. The results within this thesis will be of service in the future development of theoretical models pertaining to the interiors of γ Doradus stars.

CONTENTS

LIST OF TABLES

LIST OF FIGURES

DECLARATION

I declare that this thesis is a presentation of original work and I am the sole author unless otherwise indicated. This work has not previously been presented for an award at this, or any other, University. All sources are acknowledged as references.

In addition, I acknowledge Dr. Emily Brunsden and Dr. Duncan Wright for their substantial contribution to this thesis through the creation of the MATLAB scripts utilised for data processing. Gratitude is also expressed to Dr. Pierre Maxted for generously providing the WASP data that was invaluable for the frequency analysis in this thesis.

I would like to sincerely thank my supervisor, Dr. Emily Brunsden, for her excellent guidance.

Thomas Shutt
York, March 2018

1 INTRODUCTION

"For my part, I declare I know nothing…

But to look at the stars always make me dream."

- Vincent Van Gogh (1888)

1.1 Our Place Among The Stars

Human understanding of our place in the Universe has been tied to the stars for as long as we have existed on Earth.

Although the stars appeared to move over the course of nights, weeks and months, they always returned to their starting point. This consistency was integral to the development of agriculture, with our evolution as a species tied directly to our understanding of the rhythms of the night sky. Our culture, history, and religion are deeply entwined with the stars.

Of course, we now know that the stars are not so permanent. Aside from the proper motions that will one day distort the constellations beyond recognition, the stars themselves are evolving and in flux. On a relatively fleeting human time frame – a blink of an eye on a cosmic timescale – these variations of individual stars were unknowable until only very recently. However, developments in nuclear physics over the course of the twentieth century have led to increasingly complex models of stellar interiors, and an understanding that the life of a star is driven by the nuclear fusion in the core.

To understand the interior mechanisms of stars, we must therefore constrain the processes occurring below the surface. By observing the pulsating surface of a star, one can directly infer the processes that occur within - this is the essence of asteroseismology.

The primary goal of this thesis is to use observations of stellar pulsations to inform and constrain theoretical models, aiding in the understanding of the interior structure and excitation mechanisms of γ Doradus stars through the determination of their frequencies and modes.

This chapter introduces the reader to information useful to the understanding and contextualisation of subsequent chapters, and closes with a summary of the structure of the remainder of the thesis.

1.2 An Introduction to Asteroseismology

What we see on the surface of a star is only a small fraction of the whole. Like the motions of cogs in a clock manifests as the ticking of a pair of hands, so too do the inner workings of a star appear as regular and rhythmic pulsations on the surface. These pulsations cause brightness or radial velocity variations, which can be seen in time-resolved observations. Through spectroscopic and photometric analysis, it is possible to constrain the frequencies and modes of these pulsations and deduce the internal structure of the star.

While the desire to probe stellar interiors was first outlined in 'The Internal Constitution of the Stars' (Eddington, 1926), it required the advancement of technology and theory over the succeeding decades to really kickstart the field. Over the course of the mid-twentieth century, our understanding of quantum mechanics provided greater depth to stellar models while advancements in computing made it possible to carry out the increasingly complex calculations.

Asteroseismology as a field in its own right can trace its origins back to Douglas Owen Gough and Jørgen Christensen-Dalsgaard in the 1970s, with their work on the oscillation frequencies of the Sun. The paper 'What Will Asteroseismology Teach us' (Christensen-Dalsgaard, 1984) defined asteroseismology as:

"The Science of using stellar oscillations for the study of the properties of stars, including their internal structures and dynamics"

The variability of the star γ Doradus – the prototype star for those analysed within this thesis - was discovered by Cousins and Warren (1963) and further analysed in by Cousins and Caldwell (1989). The first suggestions of a new class came in 1993 (Krisciunas, 1993), while a more thorough classification came in at the turn of the century (Aerts, et al., 1998; Kaye, et al., 1999).

Asteroseismology is therefore built on observation and theoretical models, with beauty lying not just in the behaviour of the stars themselves, but in our analytical techniques and our attempts to interpret these observations. Analytical tools that were impossible just a few decades ago are now a powerful tool for seeing beneath the surface.

1.3 An Overview of Stellar Pulsations

Most stars, regardless of temperature and developmental stage, exhibit some variation in their luminosity (Eyer & Mowlavi, 2008), however, the most pronounced pulsational behaviour falls within (or close to) the classical instability strip on the Hertzsprung-Russell (HR) diagram, seen in figure 1.1. Fluctuations in the intrinsic luminosity of a star are caused by variation in the star's internal conditions; the release of energy trapped through opacity fluctuations in time and space. These pulsational driving mechanisms are generally a variation of the heat-engine, proposed by Eddington (Eddington, 1917), and are known as the κ-mechanism.

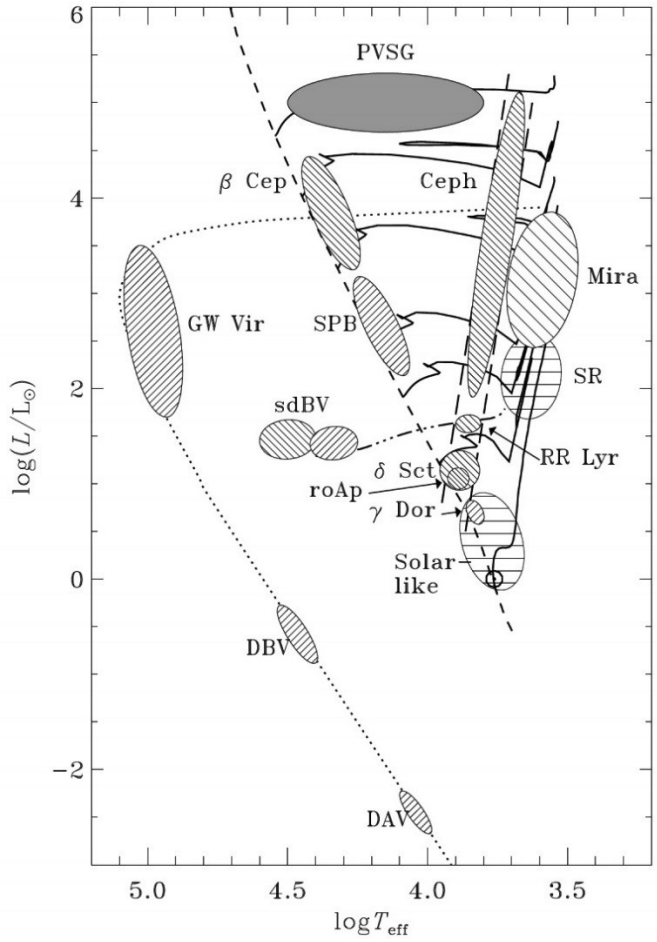

Figure 1. 1: The Hertzsprung-Russell diagram, with the γ Doradus class and the classical instability strip. Figure by Christensen-Dalsgaard (Aerts, et al., 2010).

Through this mechanism, stellar pulsations develop if a zone of partial ionisation exists in an area of the star in which the thermal time scale is comparable to the dynamic time scale (Cox, 1980). Through atmospheric compression, a rise in opacity is introduced and passage of flux from the interior is restricted. This increase in pressure and heat results in an increase in stellar radii and ionizes the hydrogen/helium gas in the region, reducing its opacity. As the opacity decreases, the gas then cools and the region contracts. As the

gas recombines, opacity is again increased and the cycle is renewed (Baker & Kippenhahn, 1962; Pesnell, 1987; Aerts, et al., 2010). A star may pulsate in two ways: radially and non-radially.

1.3.1 Radial Pulsations

Radial pulsations are characterised by the expansion and contraction of the entire star in a spherically symmetric manner, with no change in its shape – akin to a balloon into which air is pumped and then released. The number of concentric nodal shells within the star is indicated by the radial order, n. Through this definition, the fundamental mode is $n = 0$, and the first overtone is $n = 1$.

Cepheid variables, whose regular pulsations make them ideal for use as standard candles in distance measurements, are the most popularly known examples of radially pulsating stars. Cepheid's tend to pulsate in the fundamental radial mode, with the centre of the star acting as a nodal point. Through the observation of a star that pulsates simultaneously in the fundamental and the first overtone, it is possible to determine the ratio of the two modes and place infer the internal structure of the star (Aerts, et al., 2010; Schmid & Aerts, 2016).

1.3.2 Non-Radial Pulsations

Non-radial pulsations have different regions of the star expand and contract at the same time, adding transverse motion to the radial motion outlined above. Beginning with a vibrating string oscillating in one dimension, a model for these pulsations can develop, with the number of nodes increasing with the frequency. Switching into two dimensions introduces further nodes in the radial direction, and for three dimensions an additional axis is added.

From this description, nodal and anti-nodal lines can be interpreted as dividing the surface of the star into segments, defined by the azimuthal order m and the degree, ℓ. The degree, ℓ, represents the number of nodes on the surface, while the azimuthal order, m, represents the number of nodes that cross the axis of rotation. This characterisation is outlined in figure 2.1.

The orientation of a star is defined in terms of the angle between the observer's line-of-sight and the rotational axis, the inclination i. This parameter is generally difficult to measure directly, resulting in ill-defined values for rotational velocity. It is therefore necessary to introduce a minimum value for the rotational velocity of the star, a projection of the equatorial rotational velocity along the line-of-sight: $v\sin i$.

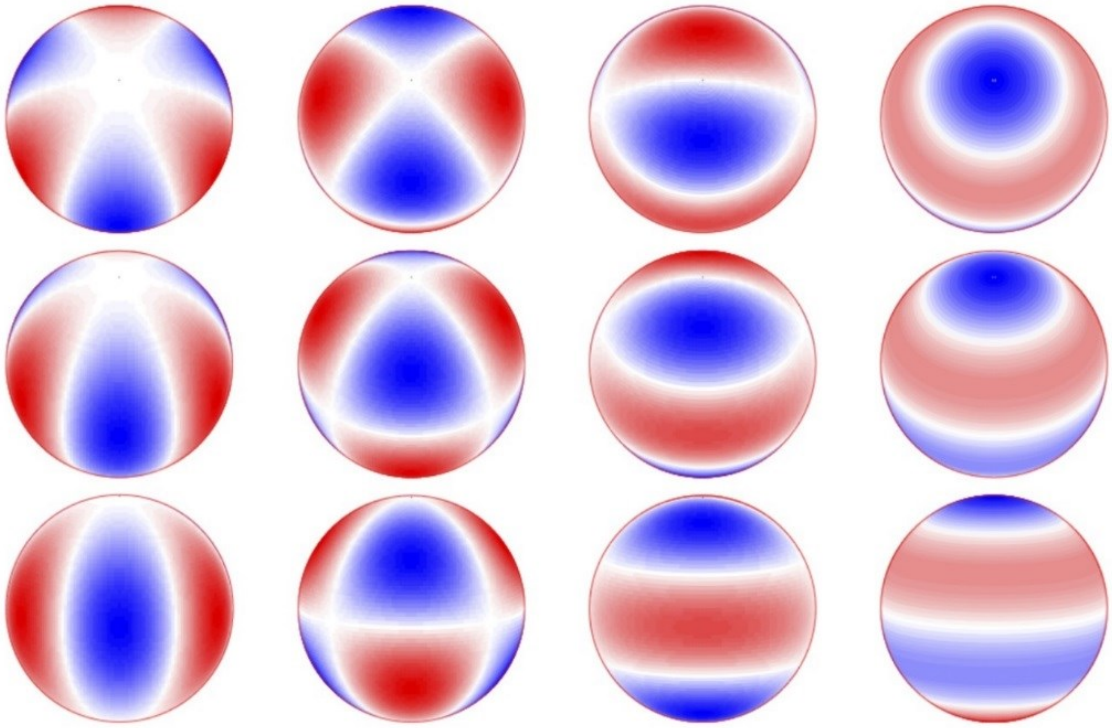

Figure 1.2: Non-radial modes viewed from three angles of inclination, from top to bottom: $i = 30°$, $i = 60°$, and $i = 90°$. The red parts represent inward motion, while the blue parts are moving outward. The intermediate white lines represent surface nodes, all of which are ($\ell = 3$) modes. The azimuthal order, m, decreases from left to right such that on the left $\ell = |m|$ and (ℓ, m) = (3, ±3), and on the right (ℓ, m) = (3, 0). Figure courtesy of Aerts et al. (2008).

The mathematical foundation on which stellar pulsations are founded is outlined in Zima (2008b) and Aerts et al. (2010), beginning with a the Legendre function:

$$P_\ell^m(x) = (-1)^m(1-x^2)^{\frac{m}{2}}\frac{d^m}{dx^m}P_\ell(x) \tag{1.1}$$

wherein $P_\ell(x)$ is the Legendre polynomial:

$$P_\ell(x) = \frac{1}{2^\ell \ell!}\left(\frac{d^\ell}{dx^\ell}(x^2-1)^\ell\right) \tag{1.2}$$

viable for $m > 0$. The spherical harmonic is defined:

$$Y_\ell^m = N_\ell^m \, P_\ell^{|m|} e^{im\emptyset} \, \cos\theta \tag{1.3}$$

Where the degree ℓ denotes the degree of pulsation (the total number of nodal lines) and m is the azimuthal order in the range $-\ell \leq m \leq \ell$ (the number of nodes intersecting with the axis). θ and $\emptyset$ are the polar and azimuthal angle in spherical coordinates and $e^{im\emptyset}$ is the complex exponential form of a trigonometric function. N_ℓ^m is a normalisation constant defined in the software FAMIAS (Zima, 2008a) as:

$$N_\ell^m = (-1)^{\frac{m+|m|}{2}} \sqrt{\frac{2\ell+1}{4\pi}\frac{(\ell-|m|)!}{(\ell+|m|)!}} \tag{1.4}$$

The pulsational modelling carried out in FAMIAS (discussed in-depth in chapter 2) assumes an alignment between the coordinate system and the spherical harmonics of the star. Although this is broadly correct for most stars (Aerts, et al., 2010), it is not true for all. The example of rapidly oscillating Ap (roAp) stars, in which the pulsation axis is aligned to the magnetic field axis is given in Kurtz et al., (2011). The assumption that stars in other classes may exhibit similar behaviour is therefore not unreasonable.

1.3.3 Types of Mode

Non-radial pulsations are subdivided into three further types: Pressure modes (p-modes) vibrate in the direction of propagation and are restored to equilibrium by pressure. They are similar to acoustic waves and their domain is the outer convective layer in cooler stars, or the radiative layer in hotter stars. The dominant pulsation generally found in δ Scuti stars, p-modes typically have frequencies in the range of 6 d^{-1} to 30 d^{-1} for stars on the main sequence (Aerts, et al., 2010).

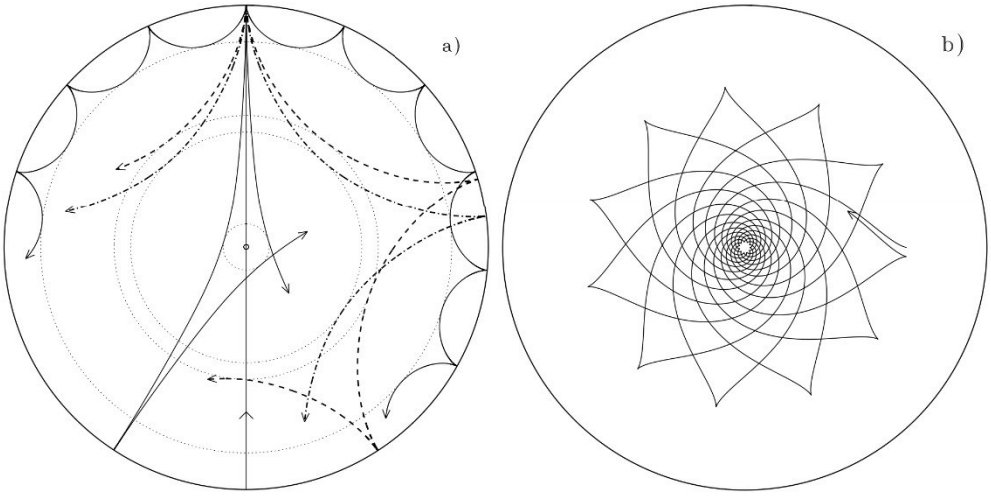

Figure 1.3: Different p-mode pulsations become increasingly refracted due to the increasing density within the star. The point at which modes of differing ℓ values are reflected is demonstrated by the concentric circles. b) A g-mode pulsation confined to the interior of the star. Diagram from Christensen-Dalsgaard (2003).

Gravity modes (g–modes) propagate perpendicular to their displacement and are returned to equilibrium via buoyancy. Lower frequencies, 0.3 d^{-1} to 3 d^{-1} for main sequence stars, are observed from g-modes (Handler, 2013). Since g-modes generally penetrate to a greater radial depth than p-modes, they are indicative of the physical

conditions deep within a star and carry with them information such as the size of the stellar core, the interior rotation profile, and variations of the sound speed in the stellar interior (Handler, 2013).

Finally, f-modes are surface gravity waves, confined to the near-surface layers of the star. The frequencies of high-degree f-modes are determined by the surface gravity and the horizontal wavelength, and depend only very weakly on the structure of the star itself (Gough, 1996).

Non-radial pulsation modes are therefore analogous to seismic waves here on Earth, and just as a seismologist is able to determine the inner structure of the Earth through earthquakes, so too can asteroseismologists use stellar pulsational modes to infer the interior structure of a non-radially pulsating star. Figure 1.3 illustrates the areas in which these modes operate.

1.3.4 The Effect of Stellar Rotation

Aside from pulsations, one of the primary contributors to the deformation of a star's structure is stellar rotation (García, et al., 2014). The main effect of this is the deviation of a star from sphericity due to rotational flattening. This has the unfortunate consequence of reducing the precision of stellar pulsation models using spherical harmonics (Reese, et al., 2006). There are currently no widely available asteroseismological models taking this factor into account.

The effect of rotation becomes notable when the period of rotation is on the same scale as the period of pulsation, this is particularly apparent for γ Doradus stars (Townsend, 2003a). Furthermore, non-radial pulsations may propagate slower than the star rotates, rendering the identification of the azimuthal order m a challenge (Townsend, 2003b). Similarly, if a retrograde pulsation propagates slower than the rotation rate, pulsations might appear prograde.

An additional consequence of rotation is rotational splitting (Cowling & Newing, 1949), wherein the rotation of a star increases the number of observed frequencies. Through this effect, the Coriolis force can result in the splitting of a single frequency into multiplets of $2\ell + 1$ frequencies. By measuring these split frequencies and any additional overtones, it is possible to determine the exterior and interior rotation rate of a star (Aerts, et al., 2010). Chapellier et al. (2012) used CoRoT data to provide evidence that space-based photometry is sufficiently precise for the identification of such frequencies in γ Doradus stars and δ Scuti stars, however, the origins of the frequency splitting are highly uncertain, with the author noting that the effects may be a result of binarity. Additionally, differential rotation, exhibited by most stars, may also imply non-uniformity in any observed splitting (Lund, et al., 2014).

1.4 Variable Stars in This Thesis

The primary concern of this thesis is the discussion of non-radially pulsating γ Doradus stars. These are of particular interest for asteroseismic investigation due to the propagation of g-modes deep into the star, allowing the probing of interior regions. These analyses in this thesis will therefore useful in the development and application of theoretical models.

1.4.1 γ Doradus Variables

γ Doradus stars are typically late A-type to early F-type stars, with approximate masses of 1.6 $M_\odot$ and radii between 1.4 $R_\odot$ and 2.4 $R_\odot$ (Kaye, et al., 1999). With temperatures of around 7200 K to 7700 K, γ Doradus stars tend to be somewhat hotter than the Sun (Handler, 1999). Guzik et al. (2000) determined that the internal structure of γ Doradus is three-layered, containing a convective core, a radiative zone, and an outer convective envelope, with pulsations driven by the κ-mechanism and convective flux blocking (Guzik, et al., 2000).

γ Doradus stars are located between the main sequence and the classical instability strip on the HR diagram (Figure 1.1) and are characterised by their g-mode pulsations of high n and low ℓ (Kaye, et al., 1999). They typically have frequencies between 0.3 d^{-1} and 3 d^{-1}, with luminosity variations of up to 0.1 magnitudes and radial velocity variations of up to several kilometres per second (Guzik, et al., 2000). The frequencies of γ Doradus stars are therefore lower than those of other A-type to F-type stars, which are between 3 d^{-1} and 80 d^{-1}.

As of March 2018, there are more than 109 well-known γ Doradus pulsators, 18 hybrids and 23 γ Doradus stars in binary systems (Ibanoglu, et al., 2018). The nature of most of these stars was originally determined from the Hipparcos mission (Perryman, et al., 1997; Aerts, et al., 1998; Eyer & Aerts, 2000). In addition to those mentioned, 291 candidate γ Doradus stars were discovered by Corot, and 307 candidates were discovered by Kepler. The number of members of this class is expected to rise through an influx of data from the upcoming TESS mission, with a current launch date listed as no later than June 2018 (NASA, 2018).

1.4.2 γ Doradus - δ Scuti Hybrid Stars

Thanks to the influx of Kepler data, an interesting subclass of pulsators has been defined, displaying characteristics of both δ Scuti stars (high-frequency p-mode pulsations) and γ Doradus stars (low-frequency g-mode pulsations). These new observations revealed 205 hybrids (Grigahcène, et al., 2010; Uytterhoeven, et al., 2011; Kahraman-Alicavus, et al., 2016; Bradley, et al., 2015).

Located between the main sequence and the classical instability strip of the HR diagram (Figure 1.1), δ Scuti stars tend to have spectral types between A and F (Rodriguez &

Breger, 2001). They are characterised by both radial pulsations and p-mode pulsations of low ℓ (Rodriguez & Breger, 2001), and typically exhibit frequencies between 3 d^{-1} and 80 d^{-1} and masses of around 1.5 to 2.5 $M_{\odot}$ (Aerts, et al., 2010). δ Scuti stars are a well-established class compared to their γ Doradus counterparts, with more than 1500 bona fide members identified (Rodriguez & Breger, 2001; Balona, et al., 2015).

In an analysis of Kepler data, Grigahcene, et al (2010) even went as far as to suggest "*there are practically no pure δ Scuti or γ Doradus pulsators*", while additional modelling of the hybrids by Balona et al. (2015) suggested that the δ Scuti class itself may need to be overhauled to incorporate mixed-mode pulsations of high and low frequencies.

It is therefore clear that additional investigation into the specific relationship between γ Doradus and δ Scuti stars is necessary for a deeper understanding of the origins of pulsations in hybrid stars. Regardless of classification, through combining p-mode data with g-mode data, it will be possible to paint a more accurate picture of the interior of these stars (Moya, et al., 2017).

1.5 Observational Asteroseismology

The primary goals of observational asteroseismology are to aid in the development of theoretical models of the interiors and pulsations of these stars. To this end, there are several large-scale campaigns to collect data on γ Doradus stars, including photometric telescopes such as CoRoT and Kepler along with several ground-based spectroscopic campaigns. Both observational avenues are crucial. A brief discussion of the observational methods, their history, and comparative strengths follows.

1.5.1 Photometry

Long periods of uninterrupted single-passband observations from space telescopes can provide many frequencies for asteroseismic analysis. The first such telescope, HIPPARCOS (High Precision Parallax Collecting Satellite), operational between 1989 and 1993, was used the purpose of astrometry and has an online database of photometric data (Perryman, et al., 1997). More recent telescopes include Corot, launched in 2006 (Baglin, et al., 2006) and Kepler, put into orbit in 2009 (Borucki, et al., 2010). In addition, ground-based broadband photometry, such as the WASP survey, can be used for long baseline, high-cadence studies of stellar variability (Smalley, 2013; Paunzen, et al., 2014).

1.5.2 Spectroscopy

The majority of the data within this thesis were collected using high-resolution spectroscopy. The expansion and contraction of the photosphere, caused by non-radial pulsations, introduces distortions across the surface of a star that manifests as asymmetric deviations across the spectral lines of a stellar spectrum. These surface-

velocity perturbations are visible as Doppler shifts - there is a blue-shift when there is expansion and a red-shift when there is a contraction.

Spectroscopy - especially high-resolution spectroscopy - is therefore invaluable for asteroseismology, with measurements able to fully characterise a pulsation mode and determine the number of nodal lines, ℓ and azimuthal number, m.

Through comparison of observed and synthetic spectra, it is also possible to constrain parameters such as the projected rotational velocity, $v\sin i$, the surface gravity, $\log g$, effective temperature, T_{eff}, and the metallicity [Fe/H]. This method is more reliable the more absorption lines a spectrum contains.

The magnitude limit for observing γ Doradus stars limits the exposure times for ground-based spectroscopic measurements. Generally, exposures in excess of 30 minutes are avoided, with the cadence becoming a substantial fraction of the frequencies being identified.

Mode identification through spectroscopy is reliant on the acquisition of large datasets, preferably from several sites to prevent effects such as aliasing – although this isn't always required (Maisonneuve, et al., 2011). The spectroscopic data available for mode identification are also limited by the allocation of observing time on these instruments. A full characterisation of the modes of pulsation is thus challenging, yet critical to the advancement of asteroseismic modelling, warranting the expense of time and resource.

There are observational advantages for selecting γ Doradus stars, with their comparatively long pulsation periods allowing for excellent temporal resolution - easily attainable exposure times of 20 to 30 minutes are in the realm of 1% to 4% of the pulsation period. However, these long exposure periods can also be a significant observational constraint. Ground-based observations from single sites mean continuous observations of a star, necessary to cover many pulsations, are impossible. Because of this, aliasing within the data is a concern.

1.5.3 Observations in This Thesis

Photometric and spectroscopic studies are complementary, and the characterisation of stellar pulsations within this thesis makes use of data from both. Two stars, HD 109799 and HD 103257, were selected as they each had several dozen archived UCMJO spectra yet to be analysed in detail, and each displayed promising variability based on preliminary analysis of HIPPARCOS data (Handler, 1999; Koen & Eyer, 2002).

1.6 Motivation and Thesis Format

The goal of this thesis is the precise determination of the frequencies and modes of oscillation for two stars. The secondary goals are to accurately constrain fundamental parameters of these stars, such as mass, radius, $v\sin i$ and inclination, i.

The remainder of this thesis is divided into four main sections. Chapter 2 introduces the methods of collecting, reducing and processing raw data, and describes the pulsation analysis techniques applied to the data to extract frequencies and modes in FAMIAS. Results for the two stars follow in Chapter 3 and Chapter 4.

An analysis of the key results, and the implications of these findings and possible future extensions is discussed in Chapter 5.

2 Data Acquisition and Processing

This chapter discusses the origin of the data used in this thesis, the methods used to bring the datasets to a state suitable for pulsation analysis and the techniques used to identify and categorise the frequencies and modes of these stars. The primary dataset used for analysis in this thesis was high-resolution spectra gathered at the University of Canterbury Mt John Observatory, augmented by photometric data from the WASP archive and the HIPPARCOS catalogue.

We begin with a discussion of the spectroscopic techniques employed.

2.1 Spectroscopic Data Collection

Spectroscopic data analysed within this thesis were collected at University of Canterbury Mount John Observatory (UCMJO), above the small town of Tekapo in the South Island of New Zealand. UCMJO – seen in Figure 2.1 – sits at coordinates of 170° 27.90 E 43° 59.20 S, at an elevation of 1029 m above sea level. Spectra were collected using the 1-metre McLellan Telescope, which is connected to the High Efficiency and Resolution Canterbury University Large Échelle Spectrograph (HERCULES) via an optical fibre of acceptance angle of 4.2° (Hearnshaw, et al., 2002).

Figure 2.1: University of Canterbury Mt John Observatory. The Dome of the 1m Mclellan telescope can be seen in the centre. The excellent site, located in the middle of an international dark sky area in the rain shadow of the Southern Alps, makes it an ideal spot for observational astrophysics. Photo by the author.

When using the 100 μm diameter fibre (as in this work), HERCULES has a resolving power of R = 41,000 (Hearnshaw, et al., 2002). Depending on seeing and wavelength, the efficiency of the spectrograph is 5 % to 15%. The CCD, a 4096 × 4096 pixel Fairchild 486 detector, enables a single exposure covering a wavelength range of 380 nm to 880nm. HERCULES is kept at a constant pressure and temperature of 0.004 atm and 20.0 ± 0.1° C respectively (Hearnshaw, et al., 2002).

2.1.1 Observational Timeframe and Target Selection

The spectra in this thesis were acquired within the remit of the MUSICIAN program (Pollard, et al., 2014) and collected over numerous observing runs, from 2009 to 2017 (Table 2.1). Two stars, HD 109799 and HD 103257, were selected as they each had several dozen archived UCMJO spectra yet to be analysed in detail, and each displayed promising variability based on preliminary analysis of HIPPARCOS data (Handler, 1999; Koen & Eyer, 2002).

Through a Royal Astronomical Society (RAS) grant, the author was able to obtain a significant number of additional spectra during observing runs at UCMJO in 2016. The remaining observations were carried out by others, with particular credit going to Mr. Fraser Gunn. The dates of observations and associated observers for the two stars are detailed in Table 2.1.

Table 2.1: The observing dates for HD 103257 and HD 109799.

Star	No' of Spectra	m_V	Exp. time (min)	Date range	Observers[6]
HD 103257	128	6.62	20	March 2009 – Jan 2017	FMG, PMK, AJG, EJB, KRP, TS
HD 109799	150	5.45	20	March 2009 – Jan 2017	FMG, PMK, AJG, KRP, TS

[6] Fraser Gunn (FMG), Pam Kilmartin (PMK), Aaron Greenwood (AJG), Emily Brunsden (EJB), Karen Pollard (KRP), Thomas Shutt (TS)

A total of 150 spectra were collected for HD 109799 at UCMJO between March 2009 to January 2017, while HD 103257 was observed from March 2009 to February 2017 and has a total of 128 observations. Characteristics of the individual stars are discussed in chapters 3 and 4.

2.1.2 Observational Methodology

Three types of spectra were recorded at UCMJO: stellar, thorium-argon and flat-field images. All of the raw data were saved as *.FITS* files, the industry standard for astronomical imaging.

The exposure times used for the stellar images varied, depending on the magnitude of the star and seeing conditions. To achieve an optimum S/N, the general observing strategy was to expose the image such that the exposure meter showed between 1.5 to 2.5 million counts, resulting in, on average, 20-minute exposures for both HD109799 and HD103257. An example stellar spectra is shown in Appendix A.

Thorium-Argon (ThAr) spectra were taken before and after each stellar image. ThAr spectra contain several thousand emission lines with well-known wavelengths and were therefore useful in the determination of wavelengths during processing. The exposure time for ThAr spectra – usually around 4 to 6 seconds – tended to vary due to the brightness of the lamp, which in turn was dependent on the input current. This was set to 7.5mA at the beginning of each nights observing. The age of the lamp also affects the brightness, with dimming over time necessitating periodic replacement. A photomultiplier tube is used to obtain counts and maintain consistency in exposures - usually between 3 and 4 million counts. An example ThAr spectra is shown in Appendix A.

Ten flat-field spectra (whites) were taken during each observing session. The flat-field spectra were obtained using an incandescent tungsten lamp and were used in combination with the ThAr's for spectral order tracing and CCD intensity response correction during processing. The white tungsten lamp is bright enough that a 1 to 2 second exposure time was sufficient to obtain well-exposed flat-field spectra. An example flat-field is shown in Appendix A.

2.1.3 HIPPARCOS and WASP Photometry

Both stars benefitted from the use of photometric data to aid in determining the validity of the spectroscopic pulsation frequencies. Photometry was from two sources: the HIPPARCOS catalogue (Perryman, et al., 1997) and the WASP archive, kindly provided by Pierre Maxted (Private communication, 2017).

The WASP instruments, located at the Observatorio del Roque de los Muchachos, La Palma and at Sutherland Observatory, South Africa, each consist of eight wide-field cameras with a 2048 × 2048 pixel CCD (Kirkby-Kent, et al., 2016). For HD103257, over 49,000 photometric measurements were available in the WASP archive, collected from 6th January 2013 to 16th July 2014. During this period, WASP-South used an 85-mm, f /1.2 lenses (Pollacco, et al., 2006; Smith & WASP Consortium, 2014).

The HIPPARCOS spacecraft used a single Schmidt telescope, with an aperture of 29 cm and superimposed two fields, separated by 58°, into a common focal plane. The system

had an astrometric accuracy of 0.002 arc-sec, and the final Hipparcos Catalogue comprised nearly 120,000 stars with a median accuracy of 1 milliarcsec. (Perryman, et al., 1997). 101 observations were present in the database for HD 103257 and 77 for HD 109799.

2.2 Processing the Raw Data

WASP and HIPPARCOS data were already fully reduced, however raw spectroscopic data from UCMJO had to be reduced for frequency and modal analysis. This was carried out through two separate MATLAB pipelines, written by Dr. Duncan Wright and Dr. Emily Brunsden (Wright, 2008; Brunsden, 2013). Although the overall reduction process remains largely unaltered, some modifications were made by the author to improve handling of the ThAr spectra and the associated calibration necessary after the opening of the HERCULES tank.

2.2.1 Reduction Pipeline 1

The first reduction pipeline identifies the type of image (Stellar, flat-field, ThAr) from the headers of the *.FITS* files and processes all images relating to each star, extracting each observation in a flux versus wavelength format. UCMJO spectra are archived based on the date of acquisition, with a month of observations generally processed as a single run.

- *Processing Flat-Field Spectra*

The initial step in processing each run was the reduction of flat-fields. This process made use of the MATLAB code *flat_processing.m*, in which flat-field spectra with exposure anomalies were discarded. The spectra were then summed to improve the signal to noise (S/N), and images were checked for substantial differences using a statistical comparison. The initial thousand rows of the CCD, corresponding to the 'blue' portion of the CCD, contained an excess of noise and were discarded.

The final output of the flat field processing stage was a reference axis, used for locating orders on the ThAr and stellar images.

- *Processing ThAr Spectra*

The ThAr images were processed using a script called *processing_all_ThArs.m.* As with the flats, a statistical comparison ensured the images were free from pixel-to-pixel deviations. Spectra affected by readout issues had to the potential to negatively impact the later wavelength calibration, so these were discarded, as were overexposed, underexposed and incorrectly saved images. In addition to the removal of the blue section of the ThAr spectra, a large portion of each image in the infra-red region was unavoidably overexposed and were not used for calibration.

On average, between 900 and 1100 calibration spectral lines were found for each ThAr spectra, depending on the variable nature of the lamp. However, if HERCULES had undergone maintenance since the creation of the most recent calibration matrix, this would manifest as a drop in emission line counts caused by a shift in the orders on the CCD. If too few emission lines were located (fewer than 800), a new calibration would be performed using the current ThAr image as a template. This new calibration would then be applied to subsequent observations.

Finally, using the axes defined by the flat-field image, a wavelength solution was created through a fourth-order polynomial fit through the positions of the spectral lines.

- *Processing Stellar Spectra*

The stellar spectra were then processed. This made use of the MATLAB code *'processing_all_stellar_images.m'*. As with the previous steps, the blue portion of the images were again removed and each stellar order was extracted using the master flat-field information.

As stellar exposure times are necessarily far longer than ThAr and flat-field spectra, the number of pixels affected by the intrusion of cosmic rays into the exposure was also far greater than in the previous steps. Correction for cosmic rays was, therefore, a two-step procedure, with an adjustment at this stage and a further correction during the continuum fitting procedure (section 2.2.3).

Since the entire system comprising the spectrograph and telescope can undergo minute physical changes over the course of the night, it was necessary to perform a linear interpolation of the wavelength solutions for the ThAr spectra either side of the stellar spectra. From this, a wavelength solution for each stellar image was determined. The data corresponding to each observation were then saved as separate MATLAB readable *.mat* files to be processed by the second data reduction pipeline.

2.2.2 Reduction Pipeline 2

The purpose of the second data reduction pipeline is to standardise the wavelength of each order across all of observations for each star; to perform a barycentric correction and a continuum fit and, finally, merge the stellar orders to produce a normalised stellar spectrum. Each spectrum is then cross-correlated with a synthetic template to produce radial velocity line profiles of each observation. This pipeline was written by Dr. Duncan Wright and Dr. Emily Brunsden (Wright, 2008; Brunsden, 2013).

Each individual observation was loaded using the script *datawork1,* which transferred the intensities onto a common wavelength axis using a spline function and formatted the data into *.mat* files.

A barycentric correction was applied to the wavelength scale, removing radial velocity variations resulting from the motion of the Earth around the Sun and the rotation of the Earth. This was calculated by calling the C script *compute barycentric* from the

spectroscopic reduction program HERCULES Reduction Software Package (HRSP) (Skuljian, 2004).

Next, order-to-order differences were removed by dividing by the median for each order and performing a polynomial fit.

2.2.3 Continuum Fitting and Spectral Order Merging

Continuum fitting normalises the stellar spectra through the identification of a continuum level of each stellar order, with a cubic spline interpolation then calculated for each order. This was done by visual comparison to a synthetic spectrum produced by the Fortran code Synspec (Zboril, 1996).

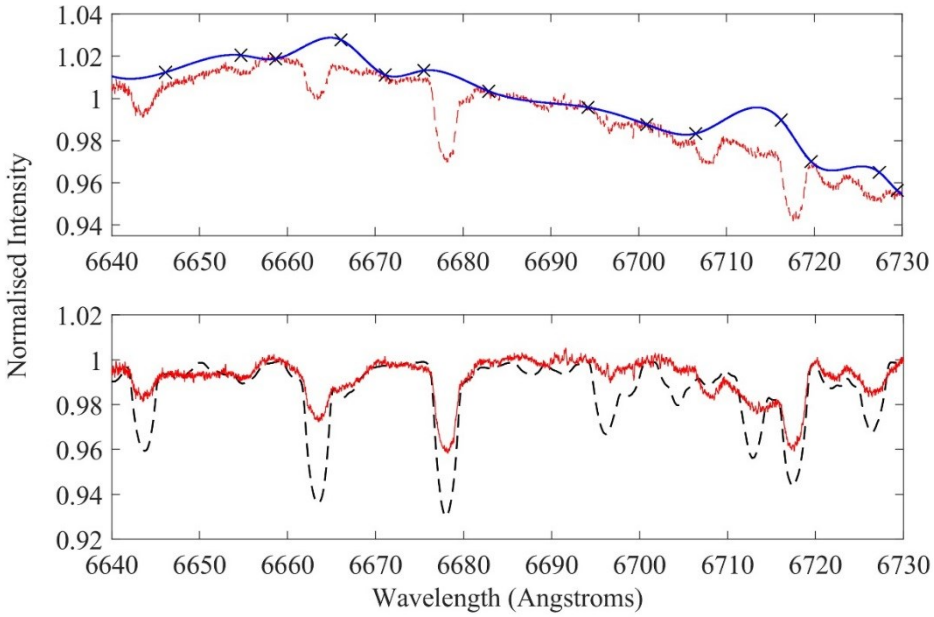

Figure 2.2: The continuum-fitting process for HD 109799. *Top:* The dashed red line is the non-continuum fitted spectral order, the black crosses are the user-defined continuum points and the solid blue line is the associated continuum level. *Bottom:* The solid red line is the normalised spectral order and the dashed black line is the synthetic spectral order generated by Synspec.

A MATLAB script called *cfitting* (Wright, 2008) plots the data and records the fit, with an example of is shown in figure 2.5. Although attempts have been made to automate this process, as of this thesis, current automation procedures introduce irregularities to the data and are best used for bulk analysis for statistical tests rather than fine analyses, with manual continuum fitting considered as a more reliable process for individual stars. After a final step to remove any remaining effects of cosmic rays, all orders are combined.

2.2.4 Cross-Correlation

Data-reduction concluded with the creation of cross-correlated line profiles for each stellar observation. By cross-correlating multiple spectral lines, the S/N is increased while retaining the periodic line-profile variations for the analyses of periodicities and mode identification. The process made use of the δ-function MATLAB code written by Dr. Duncan Wright (2008) in which the stellar spectral lines are cross-correlated with a template δ-function.

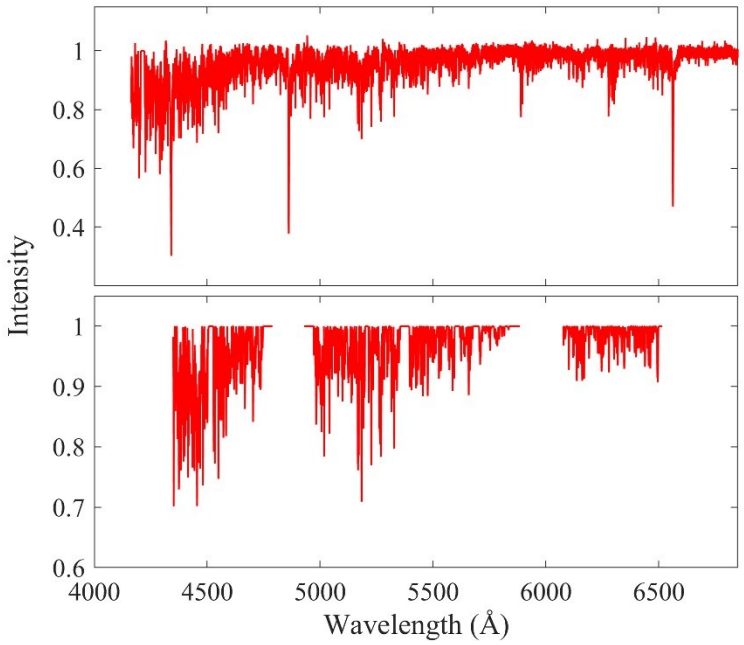

Figure 2.3: The mean stellar spectrum of HD 103257 (top) and with the telluric and weak lines removed (bottom).

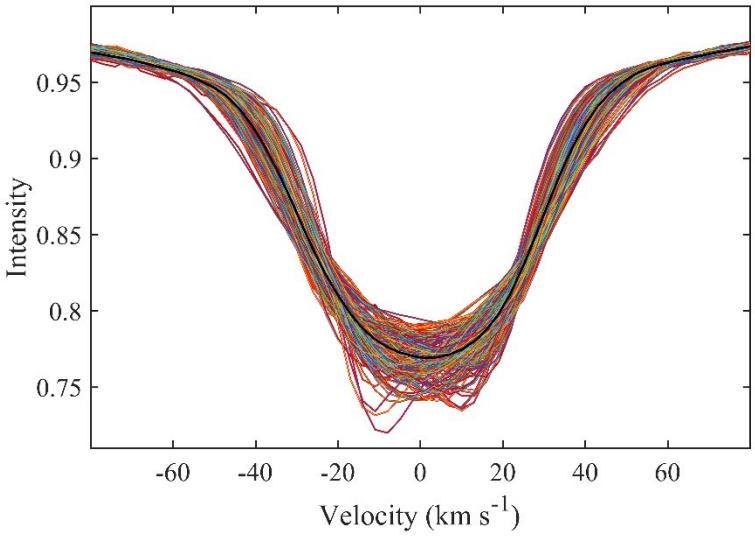

Figure 2.4: Cross-correlated line profiles of HD 109799 (multi-colour), with the mean line profile (black).

Cross-correlating telluric lines would reproduce the barycentric motion of the Earth due to their terrestrial origin, so these sections of the spectra are removed. Broad hydrogen lines (Hα, Hβ and H γ) and weak lines (small equivalent widths) were also removed as they are too noisy for reliable cross-correlations. This left approximately 2000-5000 stellar spectral lines. The final outcome of this process is illustrated in figure 2.6.

Following this step, the profiles are combined onto a single axis. The range of radial velocities of the line profiles was carefully selected for each star to incorporate the signals of the star while removing the majority of the 'wings' of the profiles, which contain little information. The cross-correlated line profiles for HD 109799 are shown in figure 2.7.

2.3 Variability Analysis in FAMIAS

Variability analysis for each of the stars was performed on the cross-correlated line profiles using the software *'Frequency And Mode Identification for AsteroSeismology'* (FAMIAS) (Zima, 2006; Zima, 2008a). Despite FAMIAS being created for the categorisation of p-modes (Desmet, et al., 2009), when used carefully it is suitable for the analysis of g-modes pulsations in γ Doradus stars (Brunsden, 2013).

The first challenge was the identification of the pulsation frequencies for each star. FAMIAS operates on the basis that pulsational frequencies are sinusoidal in amplitude and phase, performing a Fourier analysis of the line profile variations to produce Lomb-Scargle periodograms from the line profiles. These periodograms may be based on the pixel-by-pixel (PBP) method (Mantegazza, 2000; Zima, 2006) or on the moment method (Balona, 1986; Aerts & Krisciunas, 1996).

2.3.1 Comparing the PBP and Moment Methods

The PBP method analyses the movement of all pixels in a spectral absorption line, examining them as a time series the calculation of a Fourier spectrum, creating a Lomb-Scargle periodogram (Brunsden, et al., 2018). The strongest frequencies across all pixels are then identified using the mean of the Lomb-Scargle periodograms for each pixel (Lomb, 1976; Scargle, 1982)

The moment method (Balona, 1986; Aerts & Krisciunas, 1996), examines the various moments of a line profile. The equivalent width is measured by the zeroth moment; the first moment measures the radial velocity; the second moment the variance; and the third moment the skewness.

The PBP method is generally less susceptible to cancellation effects and is better at identifying frequencies with high ℓ than the moment method (Aerts, et al., 2010). In addition, it is less affected by asymmetrical line profile variation (Brunsden, 2013). For these reasons, the PBP method is regarded as the more reliable of the two methods and is the one used for this thesis.

2.3.2 Frequency Identification

The *.dat* files containing the observations for each star were first loaded into FAMIAS. To determine the frequency range for the analysis of each star, a single Lomb-Scargle periodogram was first computed using the PBP method and the frequency ranges containing most of the frequency peaks were visually identified. The initial frequency range explored covered 0 d^{-1} to 40 d^{-1}, incorporating the documented ranges for both γ Doradus and δ Scuti stars. This initial range, however, was limited by the Nyquist frequency - the minimum rate at which a signal can be sampled without introducing errors, or twice the highest frequency present in the signal (Condon & Ransom, 2016).

This frequency range was then narrowed to the visually identified range, 0 d^{-1} to 5 d^{-1} for both stars, and was used for the rest of the analysis. An algorithm then pre-whitens the first found frequency, subtracting it its variation from the whole, and allowing the discovery of additional frequencies. Pre-whitening used optimised parameters (frequency, zero-point, amplitude and phase) of the identified frequency for each pixel calculated from a least-squares fit for spectroscopic data, and the sum of the sinusoids for the photometric data. This process was iterated until no significant peaks existed above the noise floor of each periodogram. A signal to noise ratio of > 4 corresponds to a 99.9% confidence (Aerts, et al., 2010).

Figure 2.5 shows the Lomb-Scargle periodograms for the top three frequencies selected of HD 109799 using the PBP method in FAMIAS.

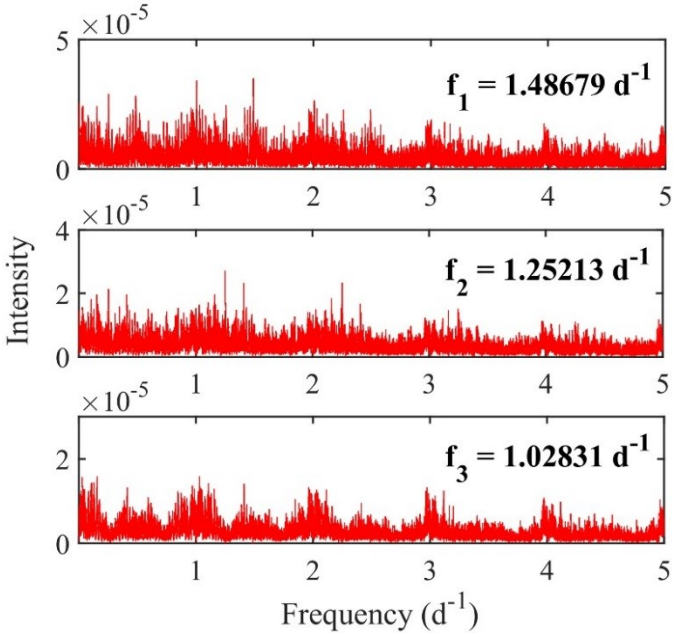

Figure 2.5: PBP mean Fourier periodograms for HD 109799, demonstrating the process of identifying and pre-whitening frequencies in FAMIAS.

2.3.3 Frequency Error Analysis

The uncertainty in a frequency is dervived by Montgomery & O'Donoghue (1999) and given as:

$$\sigma(f) = \sqrt{\frac{6}{N}} \frac{1}{\pi T} \frac{\sigma(m)}{A}, \tag{2.1}$$

where σ(f) is the standard deviation of the frequency, T is the overall time base of the observations, N is the total observations, , $\sigma(m)$ is the standard deviation of the noise and A is the mean amplitude attributable to that frequency. $\sigma(m)$ can be calculated using the following Montgomery & Odonoghue (1999):

$$\sigma(m) = \sqrt{\frac{N}{2}} \sigma(A). \tag{2.2}$$

$\sigma(A)$ is the standard deviation of the amplitude A, calculated by FAMIAS during the least-squares fitting process. By substituting this relation into equation 2.1 we can further reduce it to:

$$\sigma(f) = \frac{\sqrt{3}}{\pi T} \frac{\sigma(A)}{A} \tag{2.3}$$

The observational time base T is the total time between the first and last observation of each star, calculated by taking the difference in the Julian dates of the last (T_f) and first (T_i) observations of the star.

$$T = T_f - T_i \tag{2.4}$$

2.3.4 Final Frequency Selection

The identified frequencies for each star were then screened to identify those arising from stellar pulsations. The task of identifying these frequencies was complicated by the presence of aliasing; false frequencies introduced as a result of data sampling. A regular sampling pattern of one cycle per day (1 d^{-1}) introduces frequencies that are convoluted with the genuine pulsation stellar pulsations. This becomes an issue when the frequencies searched for exist near 1d^{-1}, as is the norm for the g-modes in these stars. Additional derivative aliases may also arise, so that 2, 3 and 4 d^{-1} frequencies may be found in the data.

This effect can be remedied somewhat by observing the star at different times each night, although this is, of course, restricted by the times at which the star is visible.

Harmonics - frequencies that are a factor or an integral multiple of any of the previously discovered frequencies - can also be troublesome. FAMIAS currently has no inbuilt protocols enabling the detection of aliases and non-exact harmonic frequencies, so their presence must be considered when selecting frequencies

In addition to removing aliases and harmonics, frequencies with irregular standard deviation profiles and any frequency peaks found below a S/N of 4 were removed.

2.3.5 Mode Identification

After a sound set of pulsation frequencies were settled upon, the next step was to identify the modal geometry of each frequency in FAMIAS. Brunsden (2013) determined the FPF method to be the most suitable when applied to spectral line profiles in relatively fast rotating stars ($v\sin i > 30$ km s^{-1}) such as those analysed herein. As such, the Fourier Parameter Fit (FPF) method was utilised in this thesis.

2.3.6 An Outline of the Fourier Parameter Fit (FPF)

The FPF technique, developed by Zima (Zima, 2006) employs a 'genetic algorithm' to explore a user-defined parameter space, searching until the parameters with the best-fit are discovered. The best-fit is established through the minimisation of the χ^2 for every fit.

The χ^2 value is a probabilistic result for, with $\chi^2 = 0$ demonstrating an ideal fit and a meaningful result is normally $\chi^2 \approx 1$. In reality, however, the χ^2 for the stars in this thesis exceed 1 due to the imperfect fitting of phase and amplitude within FAMIAS. Regardless, the final product of this process is an indication of the model with the best-fit – which is the desired result.

Modal fits in FAMIAS can be performed on the Zero-point, Amplitude and Phase profiles (ZAP) or on the Amplitude and Phase profiles (AP) only. The latter combination was selected for mode identification in this thesis since the zero-point profile has the tendency to dominate the fitting and does not distinguish well between the modes (Brunsden, 2013).

Consideration of a model's physicality is a key concern during the identification of modes, with a parameter space cultivated to exclude regions that are non-physical. For example, careful observation of the relationship between $v\sin i$ and the inclination is necessary to avoid modelling a star that approaches critical velocity wherein the star breaks apart. Obviously, the fitted mode is incorrect if this happens. This is calculated by balancing the centripetal and gravitational forces:

$$V = \sqrt{\frac{GM}{R}}. \tag{2.5}$$

Mass, M, and radius, R are found either in the literature for each star, or approximated based on average values for γ Doradus stars. G is the universal gravitational constant. Solutions are only close to the physical limit if the inclination is low ($\leq 30°$) and the $v\sin i$ is high (≥ 60 km s^{-1}) (Brunsden, 2013). If calculations approached the limit, the parameter space was amended.

2.3.7 Mode Identification Methodology

Mode identification in FAMIAS requires the input of stellar parameters: T_{eff}, log g, [Fe/H] and $v\sin i$. Although all of these parameters can be optimised in a fit, only the $v\sin i$ has any substantial effect on the shape of the synthetic line profiles (Zima, 2006). The other parameters were therefore fixed at values obtained from the literature and only the $v\sin i$ was varied.

Limb darkening coefficients, determined by central wavelength, may have an effect on the $v\sin i$ (Zima, 2008b) – however, this is fairly minimal for during the identification of modes, so the mean wavelength of the cross-correlated stellar spectra was used, set at 5000 Å (Schrijvers, et al., 1997).

An initial zero-point fit was then computed to determine the lowest χ^2 (best-fit) values for a number of stellar parameters: intrinsic width (IW), equivalent width(EW), $v\sin i$, and the velocity offset (Zima, 2008a). This computation helps to minimise the parameter space by fixing parameters that influence the shape of the line profiles for a particular star. An example of a zero-point profile is seen in figure 2.6.

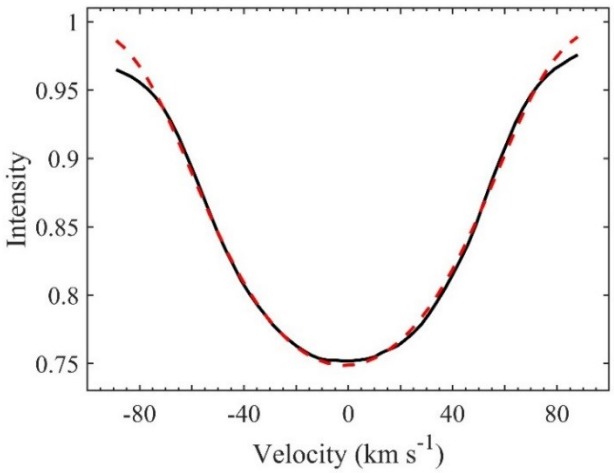

Figure 2.6: An example zero-point fit for the star HD 103257. The solid black line represents the zero-point line profile, while the dashed red line red line is the best-fit synthetic zero-point profile. This fit provided a χ^2 = 34.2.

The final - and most computationally expensive - step was to proceed with the identification of the pulsation modes for each of the determined frequencies.

The quality of the final synthetic line profile – and the speed of the computation, scaling linearly - is dictated by the number of segments of the disk FAMIAS is directed to search. For stars with a $v\sin i$ of < 30 km s^{-1}, a grid of around one thousand segments is more than adequate, while faster stars generally require over 3000 grid points to fully sample the velocity field. In addition to the degree ℓ, and azimuthal order m, the inclination, i,

stellar mass, M, and radius, R, can also be introduced as additional roaming parameters during these computations. The velocity amplitude (v.amp) and phase (φ) were also set as free parameters during the first stage of mode identification. Since the line-profile had been fit already, there was no need to repeat the process and it was omitted from further computations to facilitate a faster mode identification. An example of a best-fit pulsation mode is shown in figure 2.7.

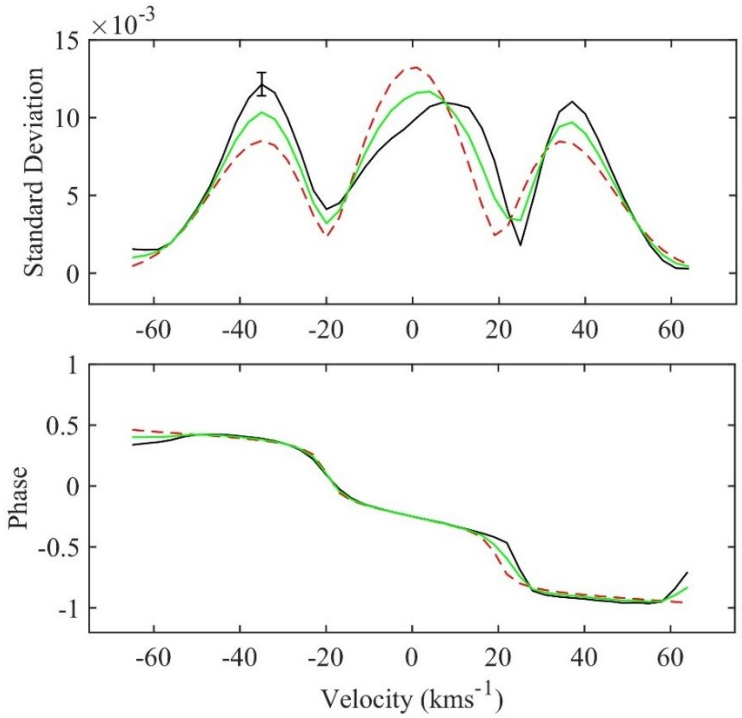

Figure 2.7: An example of the best-fit amplitude and phase profiles showing a (ℓ, m) = (1, 1) mode in the star HD 109799. The black line is the observed profile, the dashed red line is the best-fit synthetic profile, and the green represents the mean profile. The maximum statistical uncertainty is represented by the error bar.

The speed at which the modes are computed also depends on available computational capacity, or the number of CPUs. For this thesis, the load was initially shared between two computers, one with a pair of CPUs and one with four CPUs. Given the parameters outlined above and a segment space of 1000, an approximate time for two CPU's to calculate the modes for one frequency was around 20 hours, and half this for four CPUs.

Later analyses in this thesis made use of the York Advanced Research Computing Cluster (YARCC), built for the specific purpose of processing very large datasets. YARCC is a 'Tier 3' High-Performance Computing (HPC) facility consisting of 28 nodes with 56 processors and 4TB RAM. This, as one might expect, corresponded to a substantial decrease in computation times.

Finally, once the best-fit solutions for the individual frequencies were determined, ℓ, m, v.amp and φ for the best-fit mode of each frequency were set as fixed parameters and a fit with the inclination as the only variable was performed to determine if this parameter converged for each frequency.

2.3.8 Operational Limitations of FAMIAS

Modelling in FAMIAS uses the mass (M) and the radius (R) of the star to determine the *k-value*, defined as:

$$k = \frac{a_h}{a_s} \approx \frac{GM}{\omega^2 R^3}. \tag{2.6}$$

Where (a_h) is the horizontal amplitude of the pulsation, (a_s) is the radial amplitude of pulsation, ω is the angular oscillating frequency and G is the gravitational constant.

The k-value is less than one for p-modes and greater than one for g-modes. The latter generally results in pulsation frequencies that are close to 1 d^{-1} - the rotational period of a typical spectral type F star.

The mode identification in FAMIAS is limited in its ability, failing to take into consideration factors such as rotational flattening, turbulence, and granulation, while also making several assumptions in its modelling. These include a spherically symmetric unperturbed model star in hydrostatic equilibrium with no magnetic field or rotational deformation of the surface (Zima, 2008a).

The rotation of the star is also assumed to be slow enough that higher order (second-order and above) Coriolis effects can be neglected. This assumption would suggest that any mode identification for stars with a larger $v\sin i$ may be imprecise (Zima, 2008b). Despite the model star being highly idealised, these models still represent good initial solutions.

The formal operating limits of FAMIAS particular to the study of γ Doradus stars was investigated by Brunsden (2013). This work concluded that a direct impact of changing from p-modes to g-modes within FAMIAS is the requirement to increase the k-value to generate observable amplitudes of pulsation, resulting in a difference in the behaviour of the modelled mass and radius of the star. Some parameters, such as $\log g$, T_{eff}, and [Fe/H] showed limited change for variations within the γ Doradus region while modifying the mass beyond the accepted range for γ Doradus stars affected only the amplitude of the standard deviation profile. The shape of the standard deviation profile, and hence the mode identification, is not affected by the mass yet the velocity amplitude of the observed pulsation will be modified.

As such, changes to just the inclination are unlikely to affect the identification of a best-fit mode.

2.4 Summary

The spectroscopic data are novel to this work, with additional photometric data were used to support the results. The processing of the raw spectra brings them to a state that is fit for non-radial pulsation analysis, producing cross-correlated line profiles with the maximum signal-to-noise possible for each star.

Although the modelling in FAMIAS is designed for p-modes, when used with care it is suitable for the analysis of the g-modes present in γ Doradus stars.

The next two chapters describe the frequency and mode identification results for two stars: HD 103257 and HD 109799.

3 HD 103257

HD 103257 (also known as HIP 57960), is a moderately bright ($m_v = 6.62$) candidate γ Doradus star of spectral type F2V (Kahraman-Alicavus, et al., 2016). It is located between the constellations of Centaurus and Hydra at the coordinates 11h 53m 16.82s/ -36 34' 38.48'' (van Leeuwen, 2007) and is 63.37 ± 0.5 pc from Earth according to HIPPARCOS parallax measurements (van Leeuwen, 2007).

HD 103257 was designated as a γ Doradus candidate in a search for γ Doradus stars in the HIPPARCOS database (Handler, 1999), with two photometric periods of 0.817 d (1.224 d^{-1}) and 0.873 d (1.145 d^{-1}) found. HD 103257 was later categorised as an unsolved variable with a frequency of 1.22459 d^{-1} by Koen & Eyer (2002), however, no additional frequencies were confirmed.

Table 3.1 summarises the fundamental properties of HD 103257. There is currently no determined value for the radius in the literature. During the mode identification process, this was set as a roaming parameter, between the accepted values from the literature (1 $R_\odot$– 2.5 $R_\odot$). It is noted that HD 103257 is a relatively fast rotator ($v\sin i$ = 70 ± 2 km s^{-1}).

Table 3.1: A summary of the fundamental stellar parameters of HD 103257, used during spectroscopic data reduction and mode identification.

Parameter	Value used	Reference
$T_{\rm eff}$ (K)	6890 ± 95	(Wright, et al., 2003)
log g (cm s^2)	3.9 ± 0.1	(Kahraman-Alicavus, et al., 2016)
$v\sin i$ (km s^{-1})	70 ± 2	(Kahraman-Alicavus, et al., 2016)
Fe/H (dex)	-0.39	(Holmberg, et al., 2007)
Radius ($R_\odot$)	- - -	- - -
Mass ($M_\odot$)	1.40 ± 0.05	(Holmberg, et al., 2007)

3.1 Observations

Both photometric and spectroscopic data were used in the analysis of HD 103257. The principal data set comprised 128 unique spectra taken at UCMJO over a span of seven years and eleven months, from March 2009 to February 2017, with typical exposure times being 20 minutes. For cross-correlation, a wavelength range of 430 nm to 670 nm

(encompassing spectral orders 56 to 141) was used, with orders beyond this range limited in their usefulness due to contamination from hydrogen and telluric lines. Figure 3.1 shows the cross-correlated line profiles.

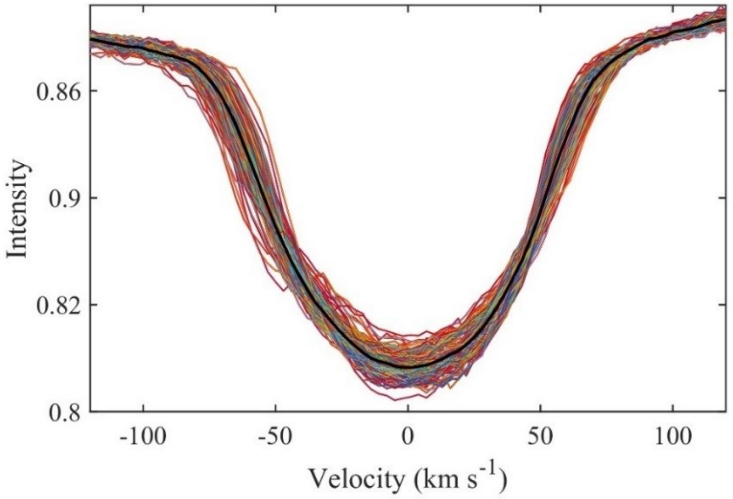

Figure 3.1: Cross-correlated line profiles (multi-colour) for HD 103257. The mean line-profile is in black.

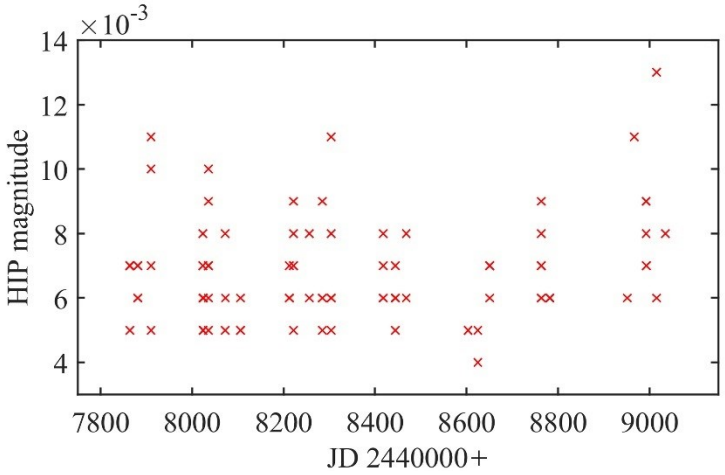

Figure 3.2: The raw HIPPARCOS data measurements for HD 103257.

UCMJO spectra were augmented by two sets of photometric data. The first was HIPPARCOS photometry (Perryman, et al., 1997), spanning a period of three years and two months, from 3rd December 1989 to 16th February 1993. During this period, 101 data points were taken using the Hp filter, seen in figure 3.2.

The second photometric dataset was WASP photometry taken at the Observatorio del Roque de los Muchachos, La Palma and at Sutherland Observatory, South Africa. A total of 49323 observations (shown in figure 3.3) were taken between 6th January 2013 and 16th

July 2014 using eight wide-field cameras with a 2048 × 2048 pixel CCD (Kirkby-Kent, et al., 2016). This dataset has not been previously analysed for frequency variations.

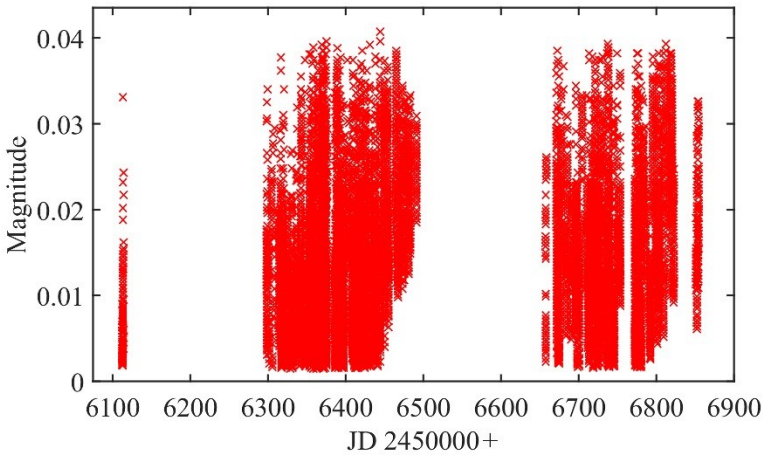

Figure 3.3: The raw WASP data measurements for HD 103257. A total of 49323 observations were taken. The magnitude of each measurement was calculated using the median flux of the entire dataset as the zero point (Kirkby-Kent et al, 2016).

3.2 Frequency Analysis

Following the procedure outlined in section 2.3.2, PBP analysis was undertaken for the LSD-derived line profiles and photometric data in FAMIAS. All discovered frequencies were pre-whitened, enabling the subsequent frequency analysis of the residuals.

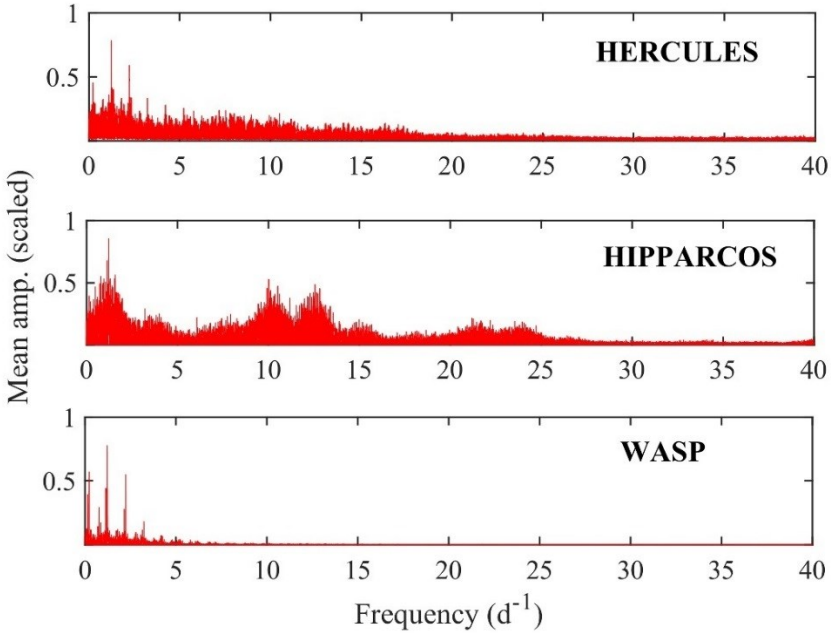

Figure 3.4: Three 0 d^{-1} to 40 d^{-1} frequency range pixel-by-pixel mean Lomb-Scargle periodograms of HD 103257 computed by FAMIAS for each dataset. Most of the variation occurs in the 0 d^{-1} to 5 d^{-1} frequency range.

To determine the frequency range where the star shows the greatest variation, an initial 0 d^{-1} to 40 d^{-1} mean Lomb-Scargle periodogram was created for each of the three data sets (Figure 3.4). Notable in the HIPPARCOS dataset is an accumulation of frequencies near 11.25 d^{-1} and multiples thereof, this being the rotation frequency of the satellite (Koen & Eyer, 2002). Based on the strong frequencies present in the WASP and HERCULES data, the 0 d^{-1} to 5 d^{-1} frequency range was selected for analysis – the region occupied by the overwhelming majority of confirmed γ Doradus stars.

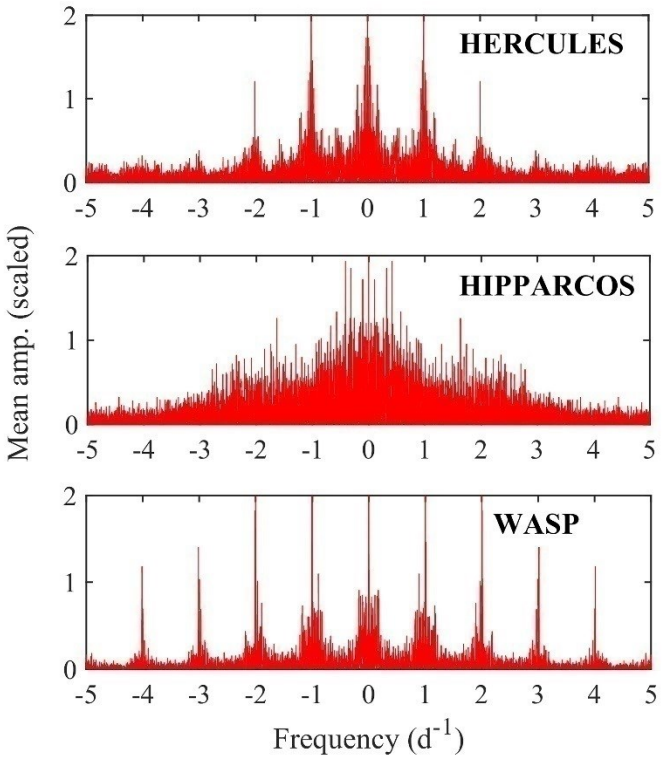

Figure 3.5: 0 to 5 d^{-1} frequency range spectral window of HD 103257 computed by FAMIAS for each dataset. Significant one-day aliasing can be seen in the HERCULES and WASP data.

Figure 3.5 shows the 0 d^{-1} to 5 d^{-1} frequency range spectral widow of HD 103257 for all three datasets, indicating the dominant frequency patterns arising from the data. Pronounced one-day aliasing is visible in both the HERCULES and WASP data, with a reassuring overlap in the HERCULES and WASP data. The Nyquist frequencies were 21.0, 13.8, and 597.2 for the HERCULES, HIPPARCOS and WASP data respectively.

3.2.1 Frequency Analysis of UCMJO Spectra

The UCMJO cross correlated line profiles were analysed for frequency identification in FAMIAS using the PBP method.

Figure 3.6 shows the first six frequencies found for HD 103257, after which further detections are were indistinguishable from the noise floor (set at S/N = 4 for the purposes of this analysis). Frequencies f_1 and f_2 dominate, accounting for 32.4% and 26.5% of the total variation of the star respectively. The peaks are clearly visible above the noise floor in figure 3.6. However, as the signal drops closer to the noise floor, aliasing within the data is further emphasised.

The PBP technique found six possible frequency peaks including an obvious one cycle-per-day alias frequency (f_5). These frequencies, their respective S/N and the proportion of the variation explained by each, are summarised in table 3.2.

Table 3.2: The frequencies found in FAMIAS using UCMJO data. Frequencies above a S/N of 4 have been reported. The uncertainty was derived using equation 2.3 using a time-base of $\Delta t = 2889$ days.

Label	Frequency (d^{-1})	Uncert. (d^{-1})	S/N	Cumulative variation explained (%)
f_1	1.22496	0.00001	18.9	32.4
f_2	1.14569	0.00002	15.5	58.9
f_3	0.67308	0.00004	7.8	66.6
f_4	0.12830	0.00004	7.1	68.2
f_5	1.06316	0.00004	5.3	76.0
f_6	1.22444	0.00005	4.4	77.0

The top two frequencies found, f_1 and f_2, accounting for 58.9% of the total variation present within the star, are repeats of the two frequencies found by Koen and Eyer (2002). All six of the frequencies found above the noise floor (S/N = 4) account for a total of 77.0% if the total variation of visible in the star.

Of note is that the ambiguity between $f_1 = 1.22496$ and $f_6 = 1.22444$ with the latter likely being residual power from the removal of the former. Figure 3.7 is a visual comparison of the standard deviation profiles for both, reaffirming the similarity. Despite the visual similarity, there was still a chance that the modes could be different – having the same (ℓ, m) values but a different n. To further test the veracity of f_6 as a frequency in its own right, the pre-whitening process was carried out on the two

frequencies individually to observe what effects, if any, removing one frequency would have on the other. In this instance, removal of f_6 prior to the removal of f_1 severely distorted the shape of the standard deviation profile for the latter, further suggesting that they are aliases. As such, given the low S/N (and associated error) of f_6, the frequency selected for modal analysis here was f_1.

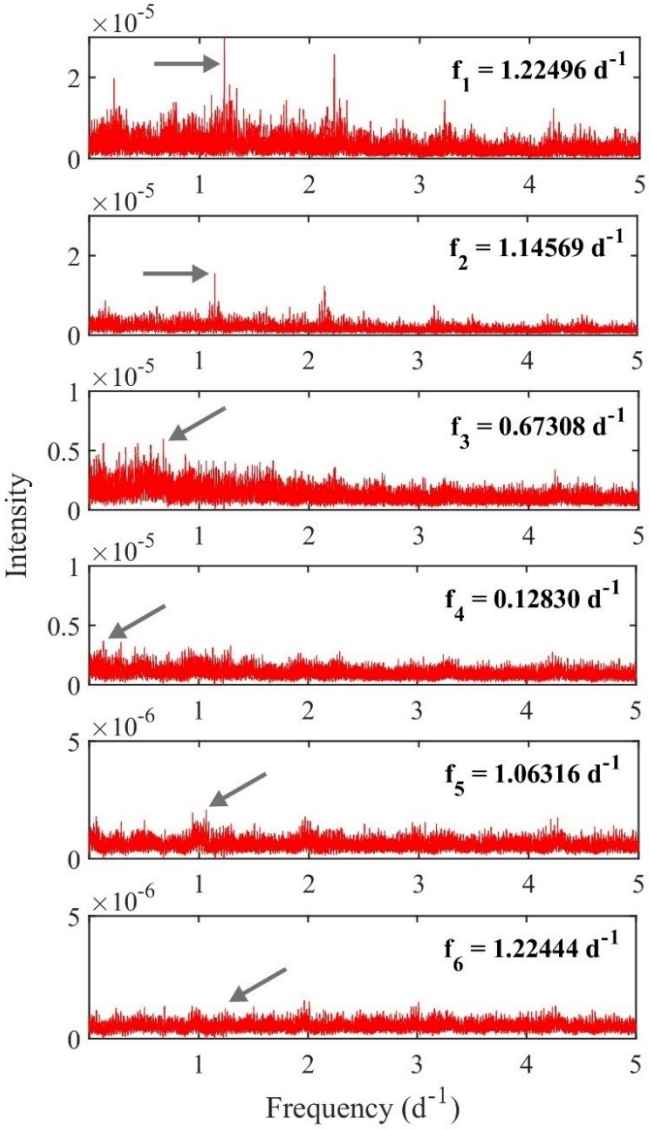

Figure 3.6: PBP mean Fourier periodograms for HD 103257 using HERCULES data, demonstrating the progressive removal of the frequency peaks. Note the shift in relative intensity scale on the latter plots, indicating a drop towards the noise floor, further emphasising the one-day aliasing due to single site observations. The arrows indicate the found frequency.

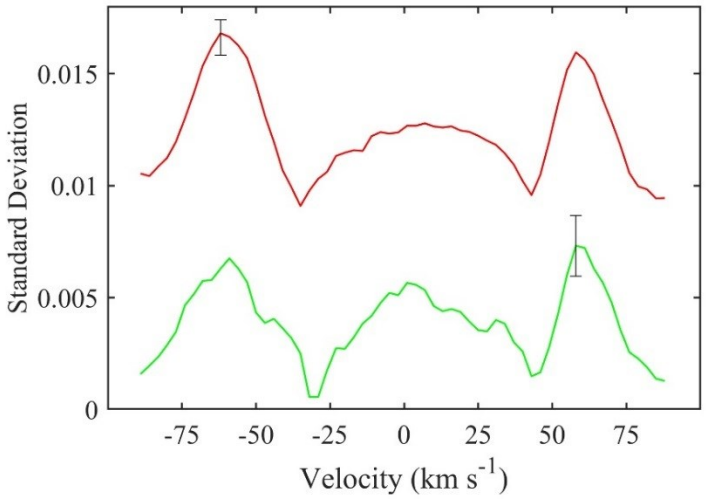

Figure 3.7: Comparison of the standard deviation curves for $f_1 = 1.22496$ (red) and $f_6 = 1.22444$ (green), reinforcing that one is an alias of the other. f_1 is offset in the y-axis for clarity. The error bar represents the maximum observational uncertainty. The aliasing was additionally reinforced through the pre-whitening of one frequency with the other.

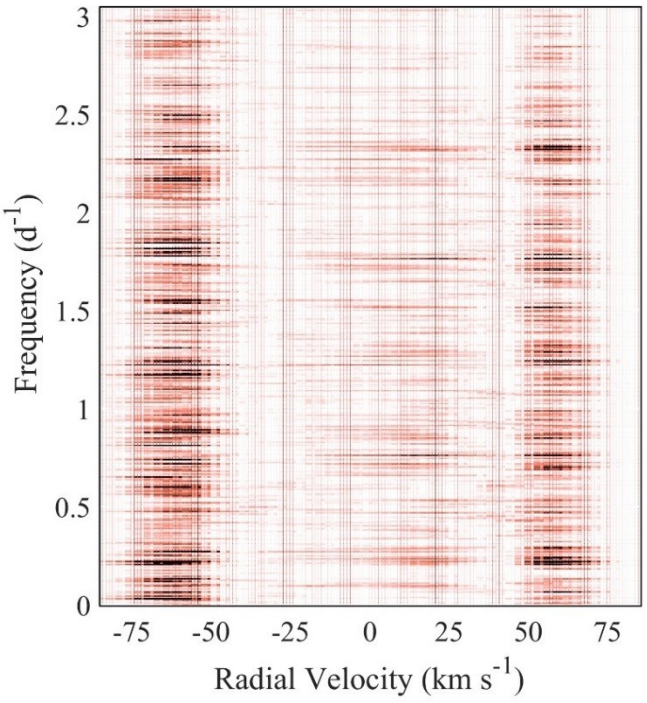

Figure 3.8: A two-dimensional PBP Fourier periodogram, with darker colours representing frequency peaks.

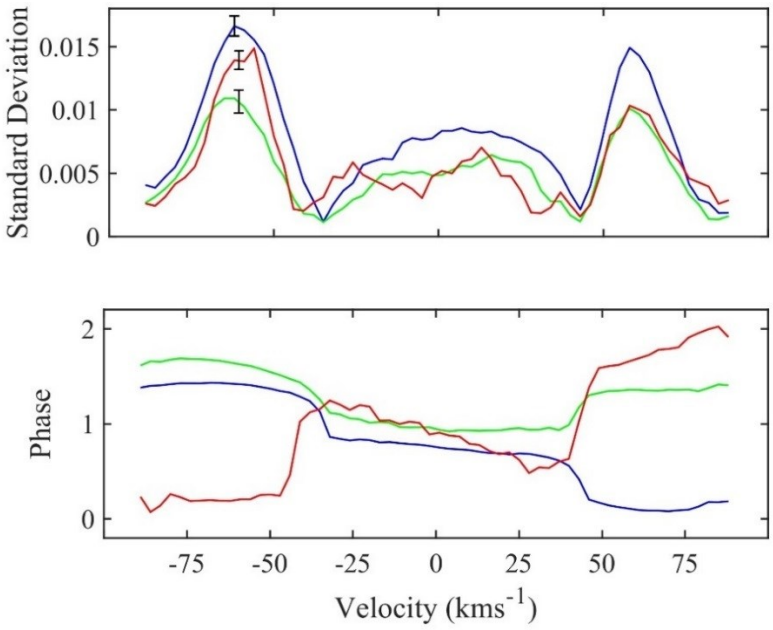

Figure 3.9: The phased, residual variations caused by the three selected frequencies from UCMJO spectra, $f_1 = 1.22496$ (blue), $f_2 = 1.14569$(green) and $f_2 = 0.67308$ (red). These frequencies account for 66.6% of the total variation observed in the star. Note that phases of ± are equivalent.

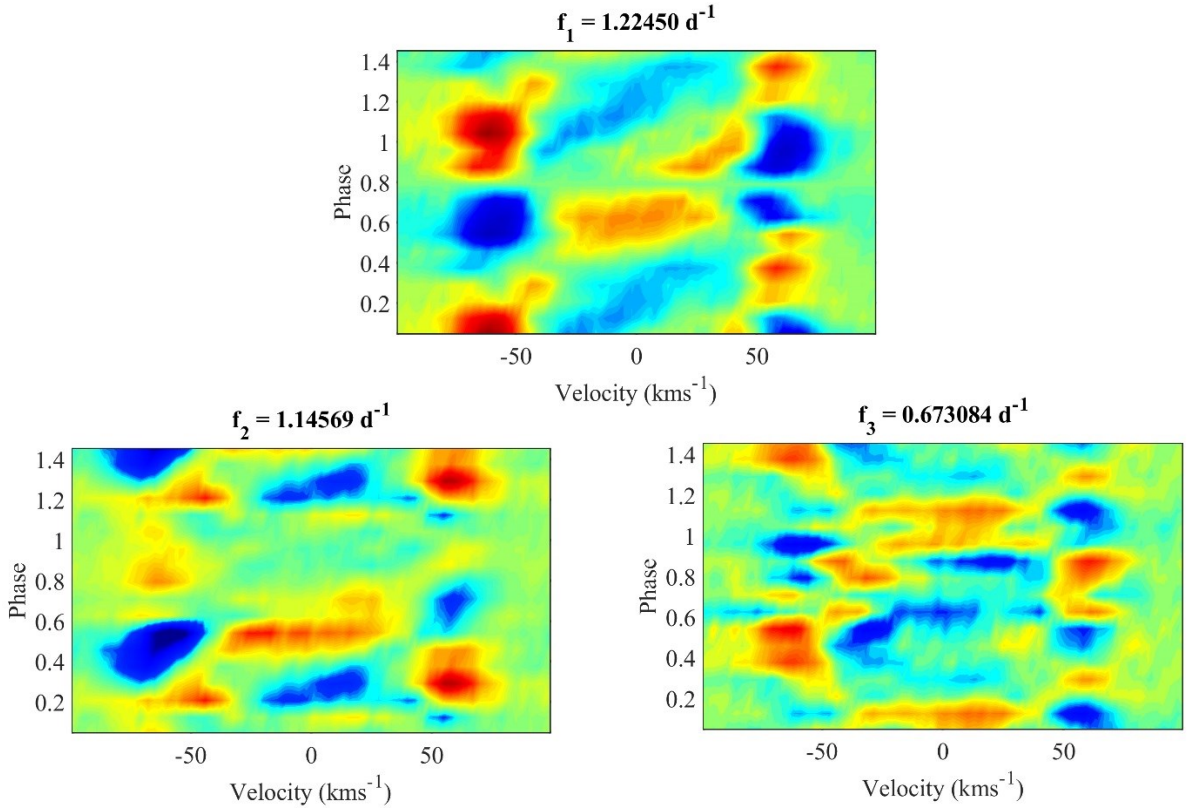

Figure 3.10: Residual line profile variations for HD 103257 phased to the top candidate frequencies, showing the typical "braided rope" structure characteristic of non-radial pulsations. The data is smoothed using a median filter.

A Fourier periodogram is shown in figure 3.8 shows, illustrating the frequency spread across all pixels. This figure shows the primary frequency (f_1 = 1.22496 d^{-1}) and its aliases dominating the pulsations.

Based on the criteria outlined in section 2.3.2, a total of five frequencies are identified as real, neglecting f_6 as an alias of f_1. Of these remaining five frequencies, only the top three are considered viable for modal analysis, with visual inspection of f_4 and f_5 demonstrating a lack of the characteristic symmetry needed for pulsation analysis.

Figure 3.9 shows the residual variations phased to the top candidate frequencies. The notable similarity in the shapes of the three profiles would suggest that a single modal type likely dominates these pulsations. The phased line profile variations for the residuals of the top three candidate frequencies are plotted in figure 3.10. These clearly show the distinctive 'braided rope' configuration that is typical for non-radial pulsations, as well as the regular changes in the blue and red wings of the line profile.

3.2.2 Photometric Frequency Analysis

The pre-whitening steps from section 3.2.1 were repeated for the HIPPARCOS and WASP data, the results follow.

3.2.3 HIPPARCOS Frequencies

The HIPPARCOS observations were screened for frequencies within FAMIAS. The HIPPARCOS data-set only comprises a comparatively low 101 observations, resulting in somewhat noisy Fourier periodograms. This is particularly evident when compared with the HERCULES and WASP spectral window plots (fig 3.6). Nonetheless, the data was sufficient to reproduce both periods found by Handler (1999) of 0.817 d (1.224 d^{-1}) and 0.873 d (1.145 d^{-1}). Beyond these frequencies ($Hf_1 = 1.2245$ and $Hf_2 = 1.1450$), it was difficult to identify convincing patterns in the frequencies beyond Hf_3. As such these are treated with caution. The frequencies found using FAMIAS, their S/N and the cumulative variation attributed to each frequency, are shown in Table 3.3.

As with the HERCULES data, the top two frequencies, Hf_1 = 1.22455 and Hf_2 = 1.14500, dominate, accounting for 47.8% and 20% of the total variation within the star respectively. Beyond these Hf_1 and Hf_2, there is a notable disagreement between the frequencies found in the HERCULES and HIPPARCOS. There is an argument to be made suggesting that Hf_4 and Hf_5 may harmonic reproductions of the HERCULES f_3

It is also noted that there is convincing evidence that $Hf_6 = 1.46101$ is a reproduction of $Hf_2 = 1.14500$, with the latter disappearing from the data if the entire dataset was first pre-whitened by the former.

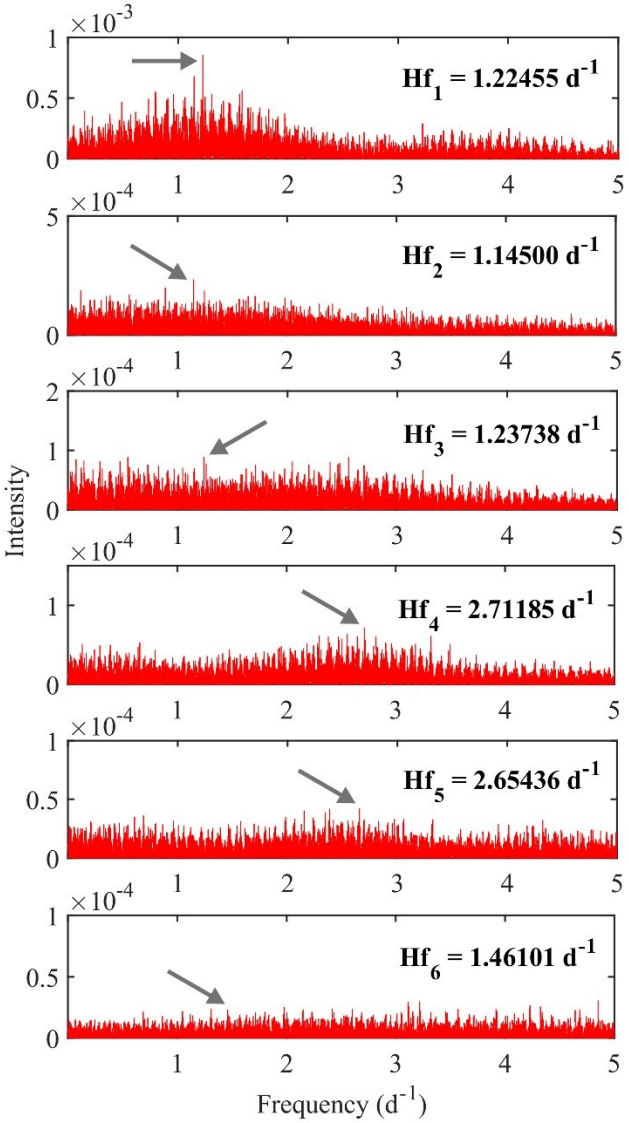

Figure 3.11: Fourier periodograms for HD 103257 using HIPPARCOS data, showing the peaks above the noise floor of S/N = 4. The arrows indicate the found frequency.

Table 3.3: HIPPARCOS frequencies above a S/N of 4. The uncertainty was derived using equation 2.3 using a time-base of Δt = 1171 days.

Label	Frequency (d^{-1})	Uncert. (d^{-1})	S/N	Cumulative variation explained (%)
Hf_1	1.22455	0.00002	26.5	47.8
Hf_2	1.14500	0.00003	23.4	67.8
Hf_3	1.23738	0.00004	14.6	66.6
Hf_4	2.71185	0.00005	11.9	71.1
Hf_5	2.65436	0.00007	9.2	77.9
Hf_6	1.46101	0.00009	6.2	81.1

3.2.4 WASP Frequencies

The 49323 WASP datapoints were screened for frequencies in FAMIASS. The benefit of dramatically increasing the amount available data for analysis is evident through direct comparison between the WASP and HIPPARCOS spectral windows, figure 3.6. Interestingly, figure 3.6 also shows that, although the data were taken at two sites, the effect of aliasing is not entirely mitigated –data taken at one site dominates.

The data were sufficient to reproduce the periods found by Handler (1999) of 0.817 d (1.224 d^{-1}) and 0.873 d (1.145 d^{-1}). Beyond these frequencies ($Hf_1 = 1.2245$ and $Hf_2 = 1.1450$), it was difficult to identify convincing patterns in the frequencies beyond Hf_3. As such these are treated with caution. The frequencies found using FAMIAS, their S/N and the cumulative variation attributed to each frequency, are shown in Table 3.3.

As with the HERCULES and HIPPARCOS data, the dominant frequencies found within the WASP data were reproductions of the two frequencies found by Handler (1999). These two frequencies, f_{W1} = 1.22486 and f_{W2} = 1.14569, account for 22.5% and 50% of the observed variation within the star respectively.

As with the HIPPARCOS photometry, beyond the first two frequencies found there is an apparent disagreement between the photometry and the spectroscopy.

Table 3.4: Frequencies above a S/N of 4, found using WASP data. The Uncertainty was derived using equation 2.3 using a time-base of Δt = 556 days.

Label	Frequency (d^{-1})	Uncert. (d^{-1})	S/N	Cumulative variation explained (%)
f_{W1}	1.22486	0.000006	17.7	22.5
f_{W2}	1.14569	0.000007	15.6	72.5
f_{W3}	0.08169	0.00002	5.5	78.5
f_{W4}	1.28905	0.00003	4.1	79.2
f_{W5}	1.20967	0.00002	4.8	82.2
f_{W6}	1.30655	0.00003	3.8	84.7

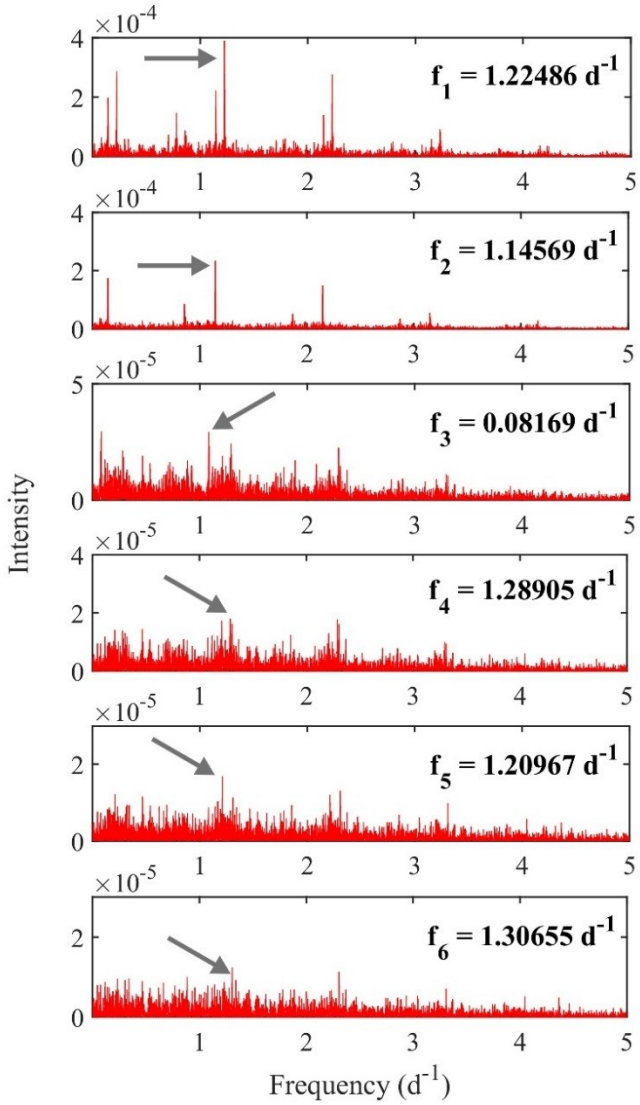

Figure 3.12: Fourier periodograms for HD 103257 using WASP data, demonstrating the progressive pre-whitening. The shift in intensity scale on the latter plots demonstrates a drop towards the noise floor. The arrows indicate the found frequency.

3.2.5 Frequency Results

It is clear from sections 3.2.1 and 3.2.2 that the first two frequencies extracted from each dataset are the most robust, appearing with clarity in each set of results. This, in combination with their appearance in the literature (Handler, 1999) makes them ideal candidates for mode identification.

Beyond these first two frequencies, however, there is notable disagreement between the photometric and spectroscopic frequencies. It is apparent that HD 103257 has as a substantial amount of the line profile variations remaining after the pre-whitening of the top two frequencies in each of the three datasets, with a maximum of 41.1% variation remaining in the HERCULES dataset and a minimum of 27.5% remaining in the WASP data.

Due to the good visual fit of the standard deviation profile for the third frequency in the HERCULES data - as well as the high $v\sin i$ for HD 103257 potentially yielding better measurement of individual pixel measurements in the spectroscopy - f_3 = 0.67308 was also selected for modal analysis.

When accounting for all frequencies found down to the noise threshold, there is still between 15.3% (WASP) and 23.0% (HERCULES) of the variation remaining for HD 103257. It is therefore highly likely that several frequencies remain undetected beneath S/N limits of the present data - to be expected given the propensity of γ Doradus stars to exhibit potentially hundreds of frequencies photometry (Brunsden, et al., 2018).

Table 3.5: The final selected frequencies to be used in modal analysis for HD 103257. The Uncertainty was derived using equation 2.3 using a time-base of Δt = 2889 days.

Label	Frequency (d^{-1})	Uncert. (d^{-1})
f_1	1.22496	0.00002
f_2	1.14569	0.00003
f_3	0.67308	0.00006

3.3 Mode Identification

Mode identification for HD 103257 followed the FPF method described in section 2.3.3. The parameters used in this step are from the literature values (table 3.1) and a zero-point fit, shown in figure 3.13. FAMIAS performed a zero-point with a χ^2 of 34.2, with the associated computed parameters summarized in Table 3.6.

Figure 3.14 illustrates the $v\sin i$ values that were explored during the zero-point fitting process. The $v\sin i$ was found to converge at 71.5 km s^{-1}, within the error expected by the literature value of 70 ± 2 km s^{-1} (Kahraman-Alicavus, et al., 2016).

Table 3.6: The zero-point fit parameters of HD 103257, computed in FAMIAS.

Parameter	Value
χ^2	34.2
Equivalent width (km s^{-1})	27.3
Intrinsic width (km s^{-1})	15.9
Velocity offset (km s^{-1})	- 1.5
$v\sin i$ (km s^{-1})	71.5

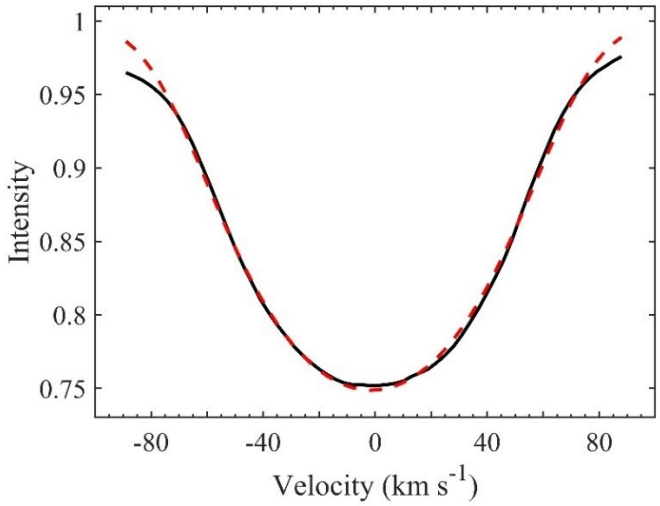

Figure 3.13: The zero-point fit of HD 103257. The solid black line represents the zero-point line profile, while the dashed red line red line represents the best-fit synthetic zero-point line profile. This fit provided a χ^2 = 34.2.

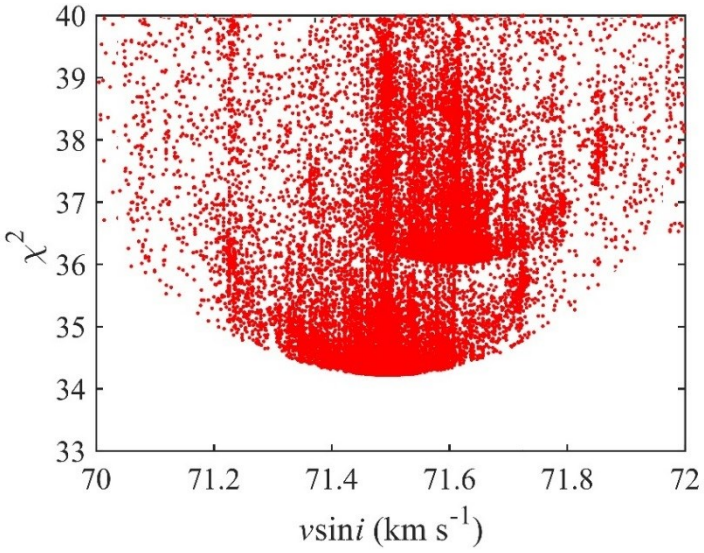

Figure 3.14: Modelled zero-point fit values for *v*sin*i*, converging on 71.5 km s^{-1}. Each red dot represents a single model.

Using the derived *v*sin*i*, and the literature value for the stellar mass, the Keplerian break up velocity and associated minimum inclination, *i*, were calculated using equation 2.5. Since no value for the radius is present within the literature, two values were derived using the upper and lower radius values common to γ Doradus stars (1 $R_\odot$– 2.5 $R_\odot$). This yielded an upper bound for the rotational velocity of v = 516.9 km s^{-1} for a star with the lower radius value, and a break up velocity of v = 326.9 km s^{-1} for the higher radius value. This provided minimum inclination values of 8.1° and 12.8° respectively. During the mode identification process, care was taken to ensure the lower bounds of any found modes were above the value at which the velocity exceeded these limits.

Due to inherent limitations in the 32-bit memory limit of FAMIAS, attempts to fit multiple modes simultaneously are unfeasible with many free parameters – particularly ℓ and m – and would result in an excessively large computation times. Instead, mode identification was first performed individually for each of the frequencies f_1 to f_3, before a simultaneous best-fit was computed using a refined parameter space while allowing the ℓ and m values to vary for each frequency. Due the status of HD 103257 as a candidate γ Doradus star, a typical parameter space for the class was searched, consisting of modes from $0 < \ell < 3$ and $-3 < m < 3$.

The absence of a value for R in the literature also left open the possibility for modelling this parameter. This was initially limited to the range R = 1 $R_\odot$ - 2.5 $R_\odot$, but was increased due to FAMIAS hitting the ceiling in the modelling and affecting the fitting of the synthetic profiles. This was then raised to an upper limit of 3.

Figure 3.15 shows the reduced χ^2 values for the models generated for each of the three frequencies. The first frequency (f_1 = 1.22496 d^{-1}) was best-fit with a reduced χ^2 value of 14.0 for an identified mode of (ℓ, m) = 1, 1 mode, while the next best-fit, a (ℓ, m) = 2, -2 had a reduced χ^2 of 20.4. The standard deviation and phase fits for the best-fit mode are seen in figure 3.16. The best-fit yielded an inclination of i = 81.3° and a radius of R = 2.6 $R_\odot$.

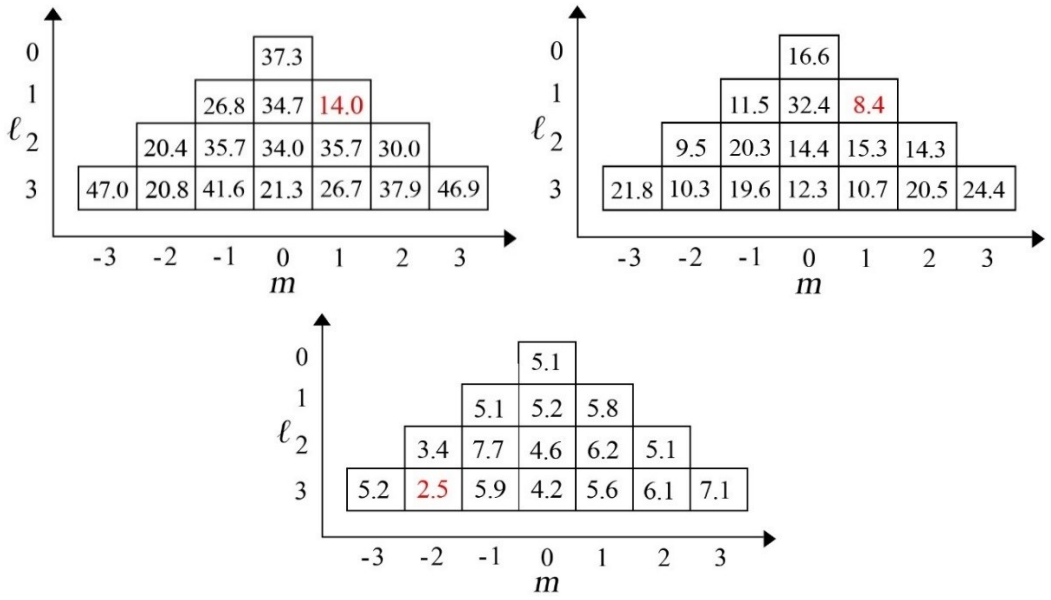

Figure 3.15: The best-fit χ^2 values for each mode for the three selected frequencies. $0 \leq \ell \leq 3$ and $-3 \leq m \leq 3$. The lowest χ^2 values are indicated in red. f_1 is top left, f_2 is top right and f_3 is bottom.

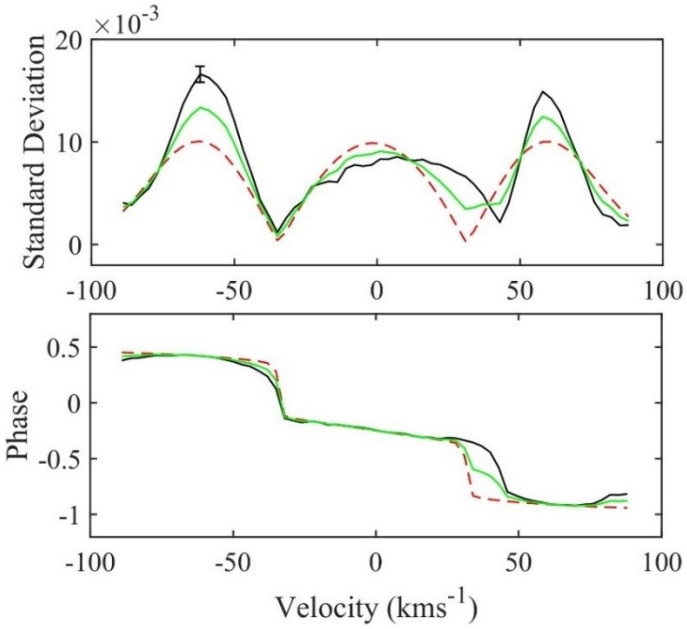

Figure 3.16: The best-fit amplitude and phase profiles for F_1 = 1.224964 d^{-1}, which is a $(\ell, m) = (1, 1)$ mode with $\chi^2 = 14.0$. The solid black line is the observed profile, the dashed red line is the best-fit synthetic profile, and the green represents the mean of the two. The statistical uncertainty is represented by the error bar.

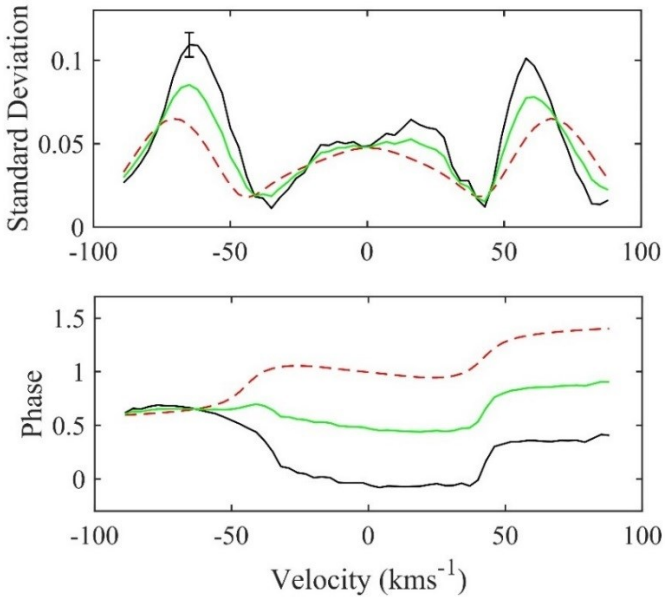

Figure 3.17: The best-fit amplitude and phase profiles for f_2 = 1.145692 d^{-1}, which is a $(\ell, m) = (1, 1)$ mode with $\chi^2 = 8.4$. The solid black line is the observed profile, the dashed red line is the best-fit synthetic profile, and the green represents the mean of the two. The maximum statistical uncertainty is represented by the error bar.

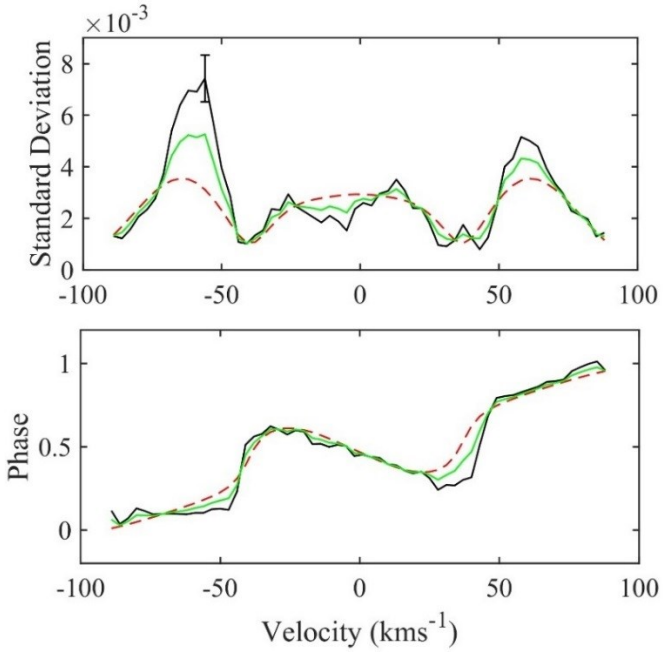

Figure 3.18: The best-fit amplitude and phase profiles for f_3 = 0.673084 d^{-1}, which is a (ℓ, m) = (3, -2) mode with $\chi^2 = 2.5$. The solid black line is the observed profile, the dashed red line is the best-fit synthetic profile, and the green represents the mean of the two. The maximum statistical uncertainty is represented by the error bar.

The modal analysis for the second frequency (f_2 = 1.14569 d^{-1}) yielded a best-fit reduced χ^2 value of 8.4 for an identified mode of (ℓ, m) = 1, 1, while the next best-fit, a (ℓ, m) = 2, -2 had a reduced χ^2 of 9.5. The standard deviation and phase fits for the best-fit mode are seen in figure 3.17. This best-fit yielded an inclination of i = 89.9° and a modelled radius of R = 2.7 $R_\odot$.

The final found frequency (f_3 = 0.67308 d^{-1}) was best-fit with a reduced χ^2 value of 2.5 for an identified mode of (ℓ, m) = 3, -2, while the next best-fit, a (ℓ, m) = 2, -2 had a reduced χ^2 of 3.4. The standard deviation and phase fits for the best-fit mode are seen in figure 3.18. The best-fit yielded an inclination of i = 34.4° and a modelled radius of R = 1.2 $R_\odot$.

Table 3.7: The individual mode identifications for HD 103257.

Frequency	χ^2	Mode (ℓ, m)	Inclination (°)	Radius ($R_\odot$)
f_1	14.0	1, 1	81.3	2.6
f_2	8.4	1, 1	89.9	2.7
f_3	2.5	3, -2	35.33	1.2

Table 3.7 summarises the individual best-fit modes of for each frequency with their associated χ^2 values, inclination and modelled radius. The ideal scenario would be for

the lowest χ^2 pulsation mode for each modelled frequency to match with respect to their respective modelled inclinations and radii, however this was not the case. Although f_1 and f_2 demonstrate strong agreement with both modelled parameters, the best-fit for $f_3 = 0.67308$ was markedly different.

A simultaneous fit for all three frequencies together was then attempted, with the varying parameters being the modes (ℓ, m), inclination, i, and the radius R. This returned a combined best-fit that repeated the individual modal analysis results for all three frequencies. This combination resulted in a best-fit with an inclination of $i = 84.6°$, $R = 2.6$ $R_\odot$ and a $\chi^2 = 10.1$. The best-fits for these are shown in figure 3.19. These results are summarised in table 3.8.

Table 3.8: Results of the combination fit for all three frequencies of HD 103257.

χ^2	f_1 (ℓ, m)	f_2 (ℓ, m)	f_3 (ℓ, m)	Inclination (°)	Radius ($R_\odot$)
10.1	1, 1	1, 1	3, -2	86.4	2.6

The difference in the outcome for f_3 compared with the individual fit is likely explained in FAMIAS' modelling of the k value. An initial value for the velocity amplitude from the individual fit of 0.7 km s^{-1} has increased for the combined fit to 4.5 km s^{-1}. This accounts for the associated increase in modelled radius, bringing it into line with the models for the two more dominant frequencies.

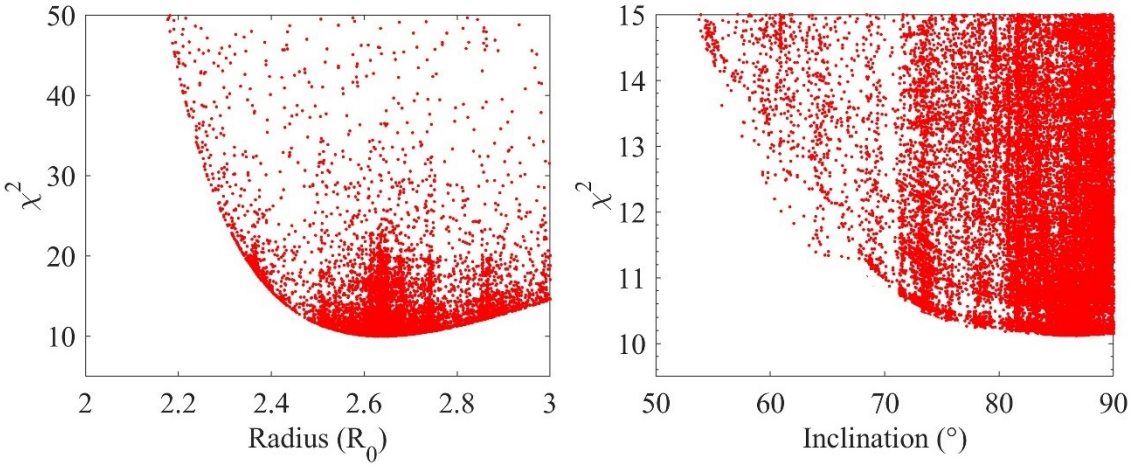

Figure 3.19: Modelled values of radius (left) and inclination (right) from the combined mode fit of HD 103257, $\chi^2 = 10.1$. The radius converged on a value of $R = 2.6$ $R_\odot$, while the inclination converged to $i = 86.4°$. Each red dot represents a single model.

Using the modelled value of radius ($R = 2.6$ $R_\odot$), a reappraisal of the Keplerian break-up velocity for HD 103257 yields a value of 320 km s^{-1}. In turn, the modelled value of inclination ($i = 86.4°$) and the derived $v\sin i$ (71.5 km s^{-1}) would have the star rotating at $v = 71.6$ km s^{-1} , well below the break-up limit.

A final point of note is that each of the synthetic standard deviation profiles for HD 103257, while having a reasonable level of fit to the observed profiles, were offset from the observed profiles by approximately 7 km s^{-1}. This effect can be seen in figure 3.20.

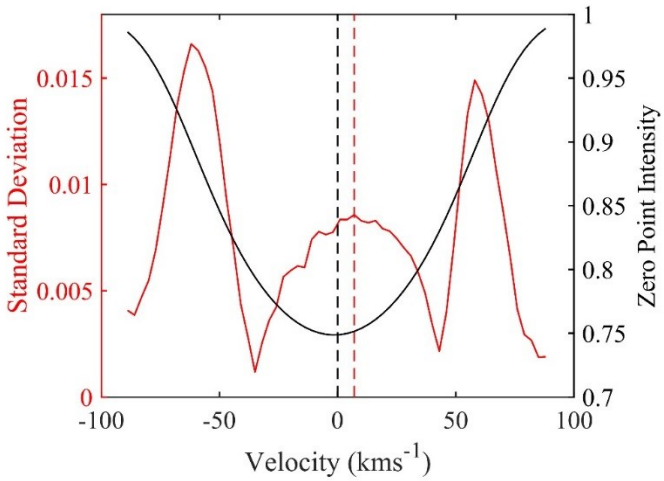

Figure 3.20: The 7 km s^{-1} velocity offset in the profile for f_3 = 1.224964 d^{-1}.

3.4 Summary

A total of 128 spectra were collected at UCMJO for frequency and pulsation analysis of HD 103257. The addition of photometric data from WASP and HIPPARCOS proved invaluable in the confirmation of the spectroscopic frequencies. Multiple frequencies were detected in each dataset, with three identified with confidence for modal analysis. The frequencies settled upon were $f_1 = 1.22496 \pm 0.00002$ d^{-1}, $f_2 = 1.14569 \pm 0.00003$ d^{-1}, and $f_3 = 0.67308 \pm 0.00006$ d^{-1}. The frequencies f_1 and f_2 were the dominant frequencies in all three datasets, accounting for 58.9 %, 67.8% and 72.5% of the variation in the HERCULES, HIPPARCOS and WASP results respectively. These two frequencies agree with those found by Handler (1999).

The confirmed modes identified for the three identified frequencies were $f_1(\ell, m) = (1, 1)$, $f_2(\ell, m) = (1,\ 1)$, and $f_3(\ell, m) = (3, -2)$ and are the first mode identifiations for pulsations within this star.

These frequencies and modes are within the typical the typical γ Doradus range of 0.3 d^{-1} to 3 d^{-1} , showing that that HD 103257 appears to be a typical γ Doradus star with variations of low harmonic degree, ℓ. Based on these results, HD 103257 can be categorised as a bona fide member of the γ Doradus class.

The modelled radius value of 2.6 $R_\odot$ is slightly higher than that typically associated with γ Doradus stars, but not unreasonable. Interestingly, the modelled inclination, i = 86.4°means that HD 103257 is viewed almost edge-on. This inclination sets the rotational velocity, v at 71.6 km s^{-1}, within reasonable bounds for an F-type star (McNally, 1965; Augustson, et al., 2012).

Since FAMIAS is unable to model pulsations that are off-axis with respect to rotation, it remains uncertain as to whether the pulsation axis of HD 103257 is aligned to that of the stars' rotation. An incongruity between the observed standard deviation profiles and the synthetic profiles for HD 103257 may be a manifestation of a misalignment and is therefore worthy of further investigation.

4 HD 109799

HD 109799 (also known as HIP 61621), is a moderately bright ($m_v = 5.45$) candidate γ Doradus star of spectral type F2IV (Alicavus et al 2016). It is located in the tail of hydra at coordinates 12h 37m 42.28s/ -27 08' 20.00'' (J2000 epoch), and is 34.3 ± 0.5 pc from Earth according to HIPPARCOS parallax measurements (van Leeuwen, 2007).

HD 109799 was designated as a γ Doradus candidate in a search for γ Doradus stars in the HIPPARCOS database (Handler, 1999), with a single photometric period found, of 1.058 d (0.945 d^{-1}) found in the data. Table 4.1 provides a summary literature values for the properties of HD 109979.

Table 4.1: A summary of the fundamental stellar parameters of HD 109799, used during spectroscopic data reduction and mode identification.

Parameter	Value used	Reference
T_{eff} (K)	6926 ± 26	(King & Schuler, 2005)
log g (cm s^2)	4.33 ± 0.11	(King & Schuler, 2005)
$v\sin i$ (km s^{-1})	39 ± 2	(Kahraman-Alicavus, et al., 2016)
Fe/H (dex)	-0.24	(Holmberg, et al., 2007)
Radius ($R_\odot$)	1.1	(Fracassini, et al., 2001)
Mass ($M_\odot$)	1.45	(Holmberg, et al., 2007)

4.1 Observations

Photometric and spectroscopic data were both used in the analysis of HD 109799. The principal data set comprised 150 unique spectra taken at UCMJO, over a time span of seven years and ten months, from March 2009 to January 2017, with typical exposure times of 20 minutes. The cross-correlated line-profiles for HD 109799 are shown in figure 4.1.

UCMJO spectra were augmented by HIPPARCOS photometry (Perryman, et al., 1997), spanning a period of three years and one month, from 4 December 1989 to 25 January

1993. This dataset comprised 78 data points, taken using a Hp filter, is shown in figure 4.2.

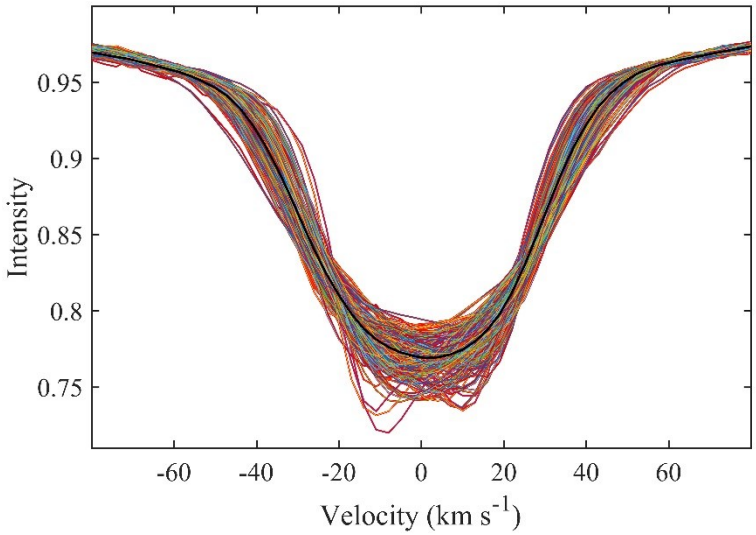

Figure 4.1: Cross-correlated line profiles (multi-colour) for HD 109799. The mean line-profile is in black.

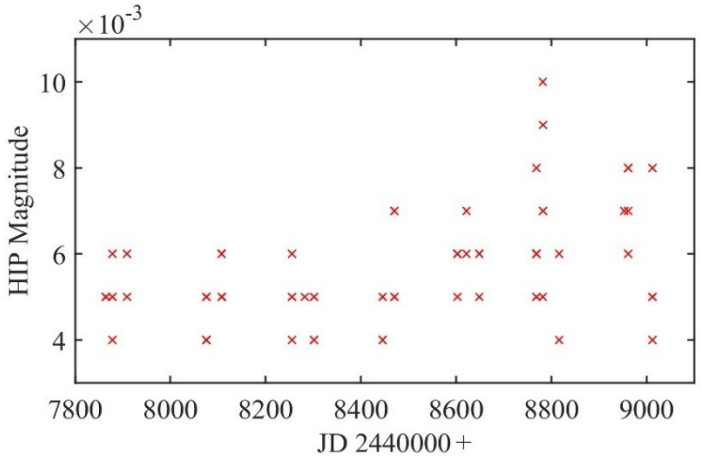

Figure 4.2: The raw HIPPARCOS data measurements for HD 109799.

4.1 Frequency Analysis

Following the procedure outlined in section 2.3.2, PBP analysis was undertaken for the LSD-derived line profiles and photometric data in FAMIAS. All discovered frequencies were pre-whitened, enabling the subsequent frequency analysis of the residuals.

An initial 0 d^{-1} to 40 d^{-1} mean Lomb-Scargle periodogram was created for each of the three data sets. This can be seen in figure 4.3. As with HD 103257, variation in the 15 d^{-1} to 25 d^{-1} was attributed to a combination of excessive noise and aliasing due to the 11.25 d^{-1} rotation frequency of the satellite (Koen & Eyer, 2002). The 0 d^{-1} to 5 d^{-1} frequency range was selected for analysis. The Nyquist frequencies were 19.7 for the HERCULES data and 13.7 for the HIPPARCOS data.

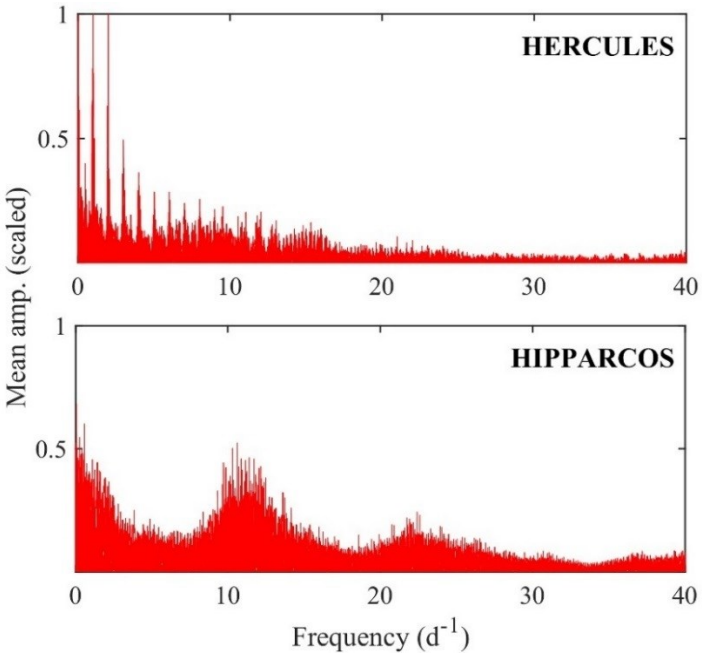

Figure 4.3: Two 0 d^{-1} to 40 d^{-1} frequency range pixel-by-pixel mean Lomb-Scargle periodograms of HD 109799 computed by FAMIAS for each dataset. Most of the variation occurs in the 0 d^{-1} to 5 d^{-1} frequency range.

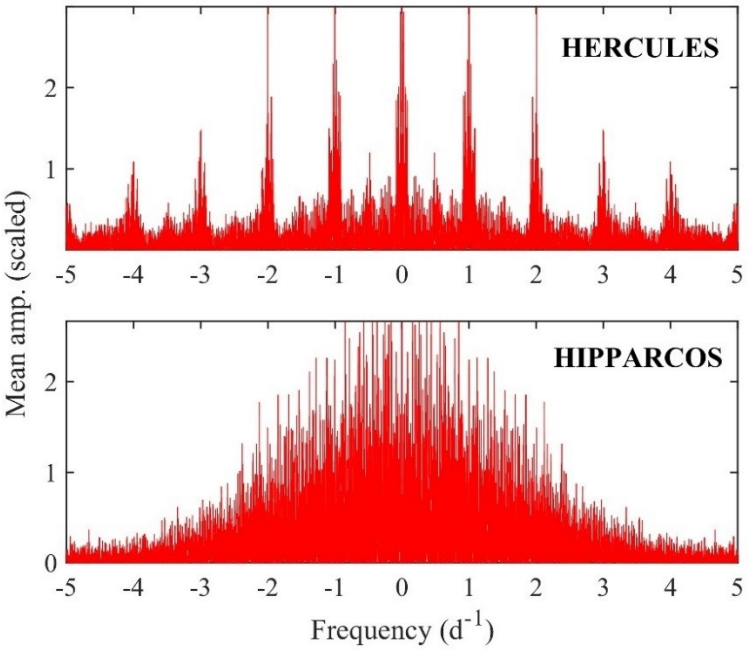

Figure 4.4: The 0 to 5 d^{-1} frequency range spectral window of HD 109799 computed by FAMIAS for each dataset.

Figure 4.4 shows the 0 d^{-1} to 5 d^{-1} frequency range spectral widow of HD 109799 for both datasets, indicating the dominant frequency patterns arising from the data sampling. Note the conspicuous one-day aliasing in the HERCULES data.

4.1.1 Frequency Analysis of UCMJO Spectra

The UCMJO cross correlated frequency identification in FAMIAS using the PBP method. This process is illustrated in figure 4.5. The PBP technique detected six frequency peaks above the noise floor of S/N = 4, listed in table 4.2.

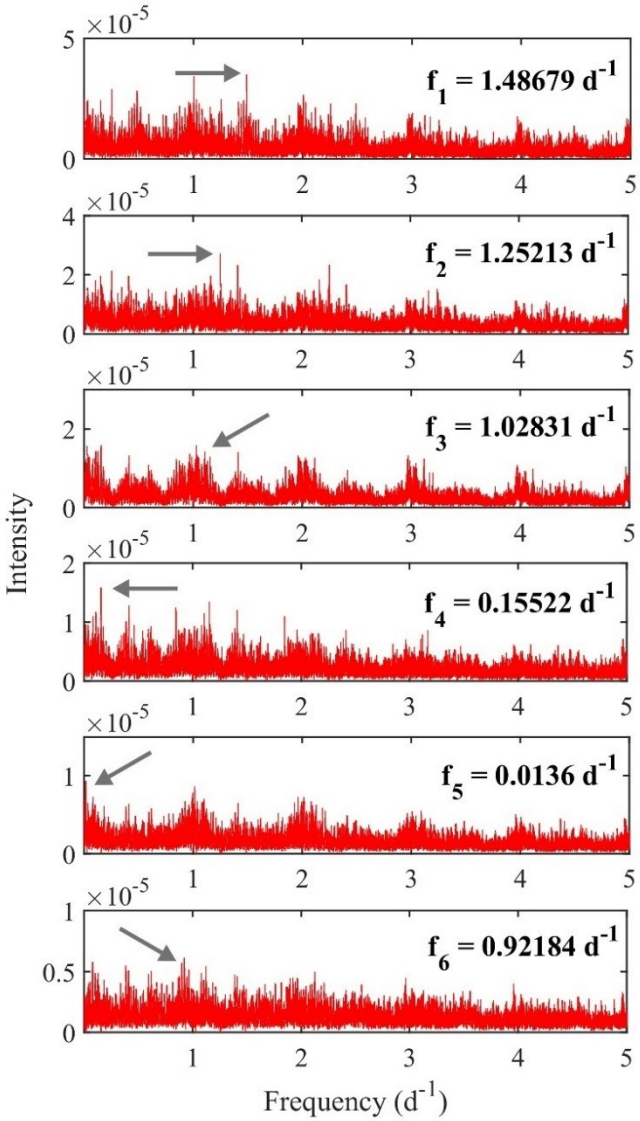

Figure 4.5: PBP mean Fourier periodograms for HD 109799 using HERCULES data, demonstrating the progressive removal of the frequency peaks. Note the shift in relative intensity scale on the latter plots, indicating a drop towards the noise floor, further emphasising the one-day aliasing due to single site observations. The arrows indicate the found frequency.

The frequencies found first by FAMIAS, $f_1 = 1.48679$ and $f_2 = 1.25213$, cumulatively account for the greatest amount of the variation within the star (32.7%) and, while the least squared fitted standard deviation plots (figure 4.6) show convincing three-bump

profiles. Additionally, the Fourier periodograms figure 4.6 clearly shows repeat peaks of $f_1 = 1.48679$ and $f_2 = 1.25213$ at one-day alias increments (0.48679, 2.48679 and 3.48679 for f_1, and 0.25213, 2.25213 and 3.25213 for f_2), further emphasising the strength of these frequencies.

Table 4.2: Frequencies found using UCMJO data. The uncertainty was derived using equation 2.3 using a time-base of $\Delta t = 2861$ days.

Label	Frequency (d^{-1})	Uncert. (d^{-1})	S/N Ratio	Cumulative variation explained (%)
f_1	1.48679	0.00002	7.2	11.8
f_2	1.25213	0.00002	8.2	32.7
f_3	1.02831	0.00003	5.2	32.6
f_4	0.15522	0.00003	8.4	48.2
f_5	0.0136	0.00003	4.2	58.1
f_6	0.92184	0.00004	4.5	64.7

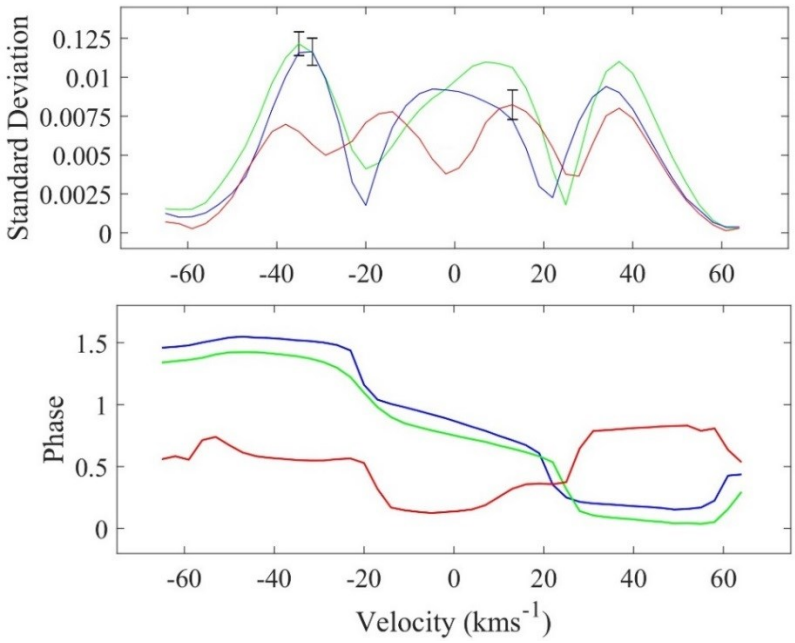

Figure 4.6: The phased, residual variations attributed to the top three selected frequencies from UCMJO spectra, $f_1 = 1.486792$ (blue), $f_{h2} = 1.252126$ (green), and $f_6 = 0.92184$ (red). These frequencies account for 39.3% of the total variation observed in the star. Note that phases of ± are equivalent.

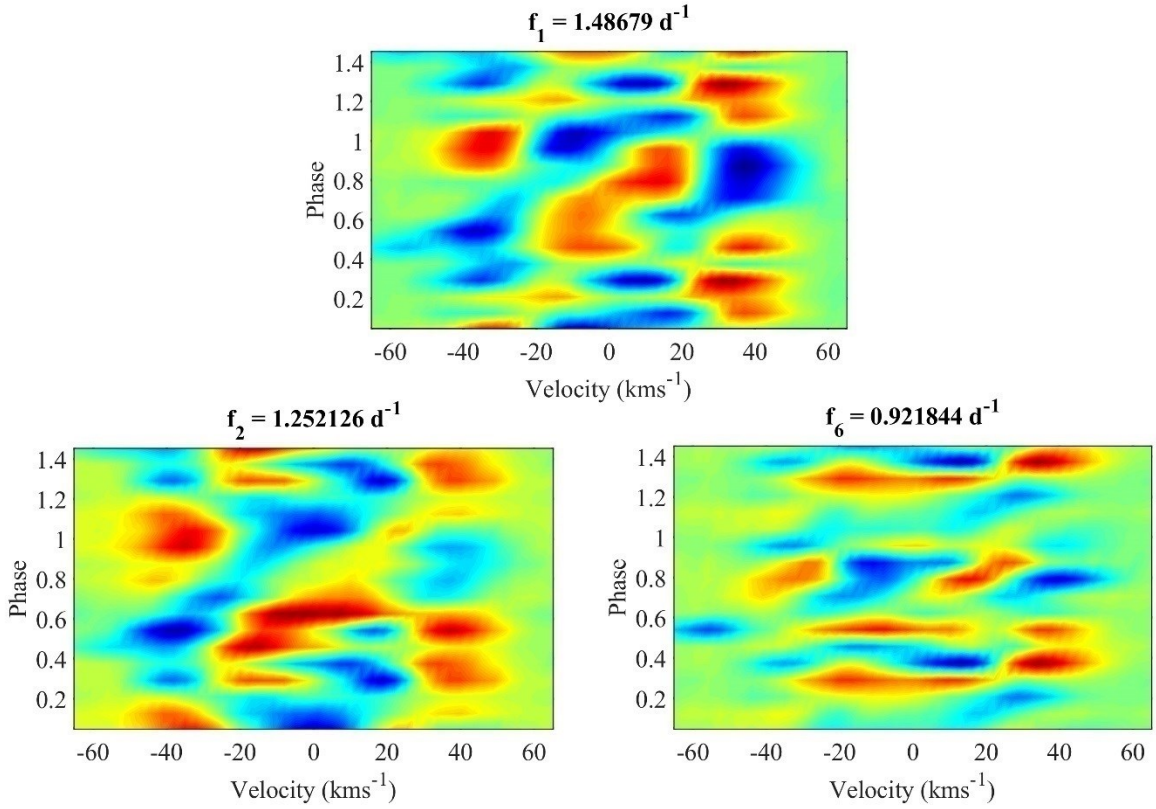

Figure 4.7: Residual line profile variations for HD 109799 phased to the top candidate frequencies, showing the typical "braided rope" structure characteristic of non-radial pulsations. The data is smoothed using a median filter.

Of note is the reappearance of the frequency recorded by Handler (1999) in the form of $f_6 = 0.92184$. Although it was the sixth frequency found, this accounts for over 6% of the total variation within the star. Indeed, when pre-whitening the raw data using this frequency first, f_3 disappeared from the list.

Of the remaining frequencies found, f_5 appears to be a one day alias, while visual inspection of the standard deviation profile for f_4 shows no non-symmetric variation.The phased line profile variations for the residuals of the top three candidate frequencies are plotted in figure 4.7, with the 'braided rope' structure apparent for f_1 and f_2, but notably distorted for f_6.

4.1.2 Hipparcos Frequencies

The HIPPARCOS observations were screened for frequencies in FAMIAS. The HIPPARCOS data-set only comprises a comparatively low 77 observations, resulting in somewhat noisy Fourier periodograms, however this was sufficient to reproduce the period found by Handler (1999) of 0.945. Categorisation of frequencies found beyond this was unsuccessful. The frequencies found, and their S/N, are shown in Table 4.3.

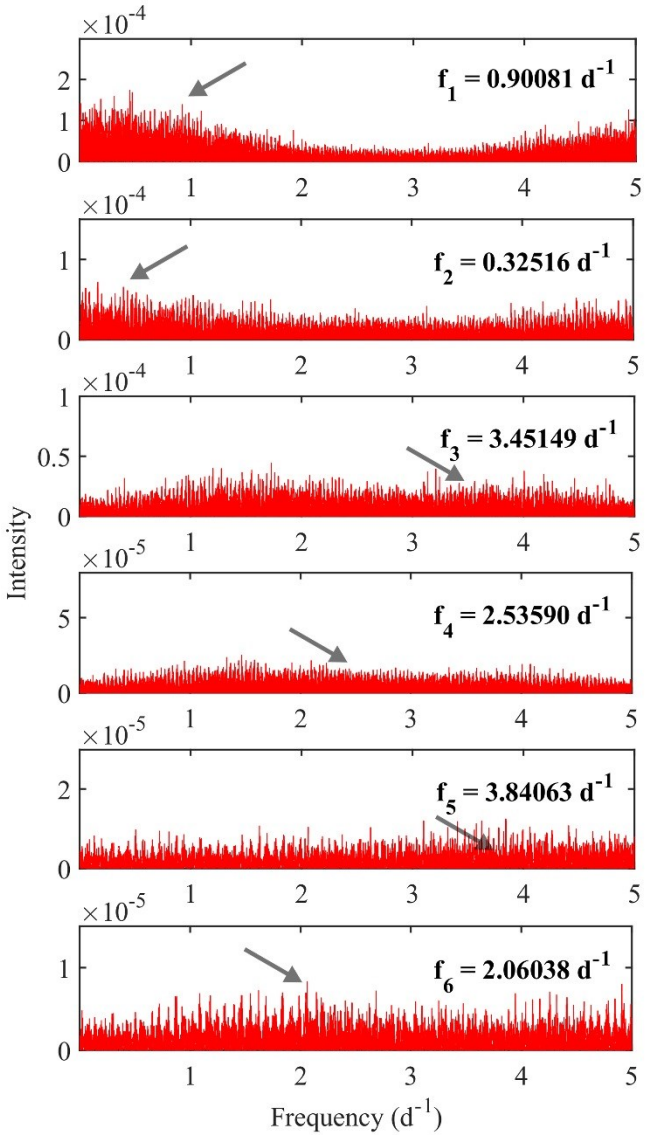

Figure 4.8: Fourier periodograms for HD 103257 using HIPPARCOS data, for peaks above the noise floor of S/N = 4. The arrows indicate the found frequency.

It is noteworthy that initial analysis of the HIPPARCOS data failed to reproduce the frequency found in the earlier analysis (Handler, 1999), and only when several outlying data-points were removed did the frequency of $Hf_1 = 0.9008$ materialise. The similarity between this frequency and f_6 in the HERCULES data is noted. Indeed, when the HERCULES data was pre-whitened to include the frequency $Hf_1 = 0.9008$, the standard deviation profile for the equivalent spectroscopic frequency, $f_6 = 0.92184$, was severely warped – suggesting a relationship between the two.

Beyond this first frequency, however there appears to be disagreement between the HERCULES and HIPPARCOS analyses. It is possible that $Hf_3 = 3.45149$ is a repeat of $f_1 = 1.48679$ from the HERCULES data. Indeed, pre-whitening of the spectroscopic data with $Hf_3 = 3.45149$ brings out the same shaped profile, while the variations from the other disappear if they are pre-whitened simultaneously.

Table 4.3: Frequencies found using HIPPARCOS data above a S/N of 4. The uncertainty was derived using equation 2.3 using a time-base of Δt = 1148 days.

Label	Frequency (d^{-1})	Uncert. (d^{-1})	S/N Ratio	Cumulative variation explained (%)
Hf_1	0.90081	0.00004	15.3	35.8
Hf_2	0.32516	0.00006	11.8	49.5
Hf_3	3.45149	0.00005	14.3	61.9
Hf_4	2.53590	0.00007	9.7	73.2
Hf_5	3.84063	0.0001	5.9	78.1
Hf_6	2.06038	0.0001	6.3	84.5

It is also plausible that $Hf_2 = 0.32516$ is a 2x harmonic of $f_4 = 0.15522$ from the UCMJO data.

4.1.3 Frequency Results

The discrepancy between the frequency f_6 = 0.92184 d^{-1} (HERCULES) and $Hf_1 = 0.90081$ d^{-1} (HIPPARCOS) may be accounted for due to the inherent noise inherent to the HIPPARCOS data. Nonetheless, the proximity of the two frequencies to that found by Handler (1999), F = 0.945 d^{-1}, would suggest that all three are one and the same, and modal analysis was pursued with caution.

Table 4.4: The final selected frequencies to be used in modal analysis for HD 109799. The uncertainty was derived using equation 2.3 using a time-base of Δt = 2861 days.

Label	Frequency (d^{-1})	Uncert. (d^{-1})
f_1	1.48679	0.00002
f_2	1.25213	0.00002
f_6	0.92184	0.00004

Additionally, the first two frequencies found in the HERCULES analysis (f_1 = 1.48679 d^{-1} and f_2 = 1.25213 d^{-1}) demonstrate excellent S/N and robust variation in their standard deviation profiles. The former is also repeated in the HIPPARCOS data in the guise of Hf_3 = 3.45149, the frequency in that dataset with the second highest S/N. As such, the two first HERCULES frequencies are also selected for modal analysis.

It is apparent that HD 109799 has as a substantial amount of the line profile variations remaining after removal of the selected frequencies in both the HERCULES and HIPPARCOS data. The three selected frequencies in the former account for 39.3% of the total variation, meaning it is highly likely that several additional frequencies remain undetected beneath the S/N threshold of the data.

4.2 Mode Identification

Independent mode identification for HD 109799 followed the FPF method described in section 2.3.3. The parameters used in this step are from the literature values (table 4.1) and a zero-point fit, shown in figure 3.9. FAMIAS performed a zero-point with a χ^2 of 24.3, with the associated computed parameters summarized in Table 4.5.

Figure 4.11 illustrates the $v\sin i$ values that were explored during the zero-point fitting process. The $v\sin i$ converged at 40.2 km s^{-1} with a χ^2 of 24.3, reassuringly close to the literature value of 39 ± 2 km s^{-1} (Kahraman-Alicavus, et al., 2016).

Table 4.5: The zero-point fit computed parameters of HD 109799**.**

Parameter	Value
χ^2	24.3
Equivalent width (km s^{-1})	15.6
Intrinsic width (km s^{-1})	17.4
Velocity offset (km s^{-1})	-0.2
$v\sin i$ (km s^{-1})	40.2

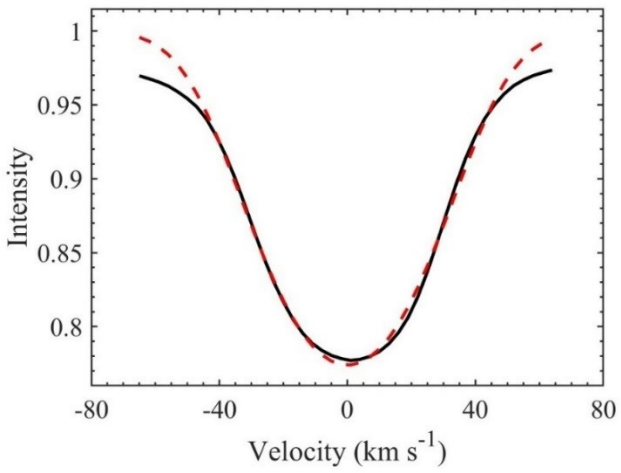

Figure 4.9: The zero-point fit of HD 109799. The solid black line represents the zero-point line profile, while the dashed red line represents the best-fit synthetic zero-point line profile. This fit provided a χ^2 = 24.3.

Throughout modal analysis, the value for the inclination parameter space was set to be above that at which the rotational velocity surpasses its upper limit. Using equation 2.5, radius and mass values of $R = 1.1\ R_{\odot}$ and $M = 1.45\ M_{\odot}$ (Fracassini, et al., 2001; Holmberg, et al., 2007) and a $v\sin i$ of 40.2 km s^{-1} (table 4.5), a critical velocity and lower limit for inclination were 501.5 km s^{-1} and 4.6° respectively.

Mode identification was performed individually to find the best-fit for each of the frequencies, before a simultaneous best-fit was performed for all frequencies together, using a refined parameter space. Due the status of HD 109799 as a candidate γ Doradus star, a parameter space typical for the class was searched, consisting of modes from $0 < \ell < 3$ and $-3 < m < 3$.

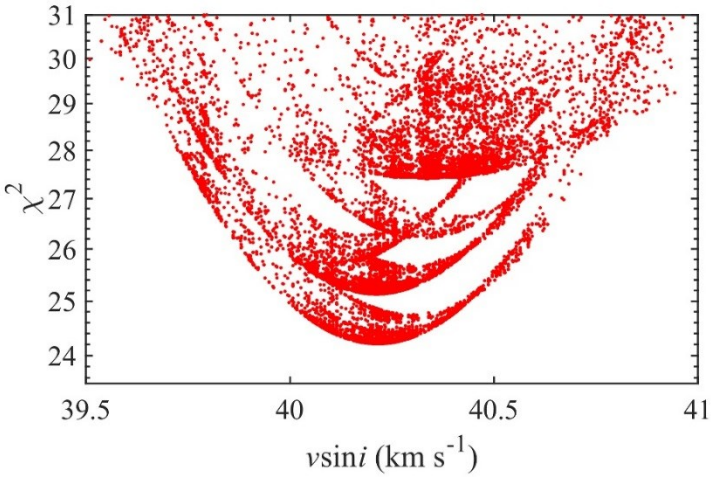

Figure 4.10: Modelled zero-point fit values for $v\sin i$, converging on 40.2 km s^{-1}. Each red dot represents a single model.

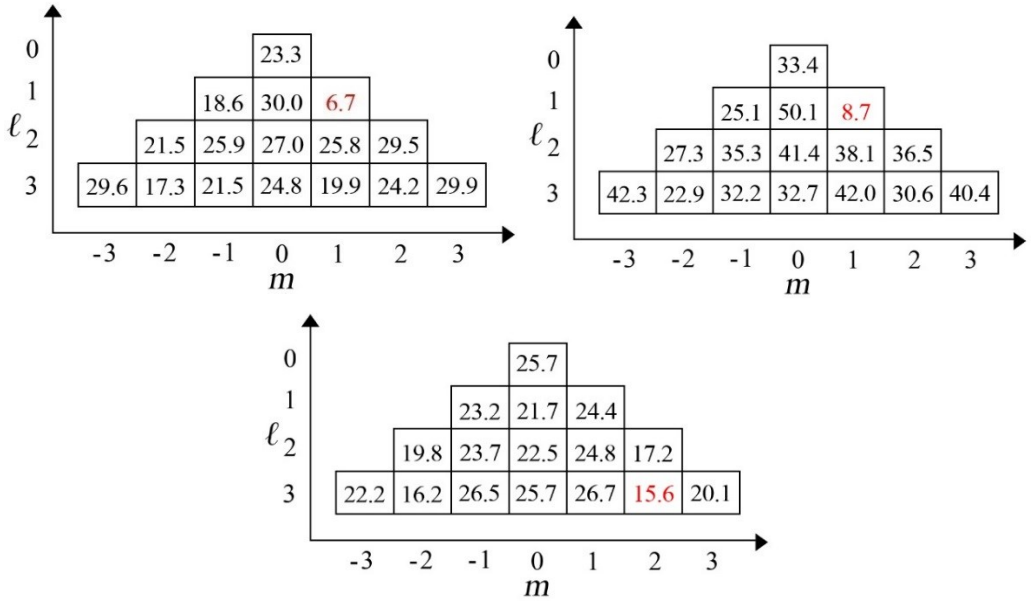

Figure 4.11: The best-fit χ^2 values for each mode for the three selected frequencies. $0 \leq \ell \leq 3$ and $-3 \leq m \leq 3$. The lowest χ^2 values are indicated in red. f_1 is top left, f_2 is top right and f_6 is bottom.

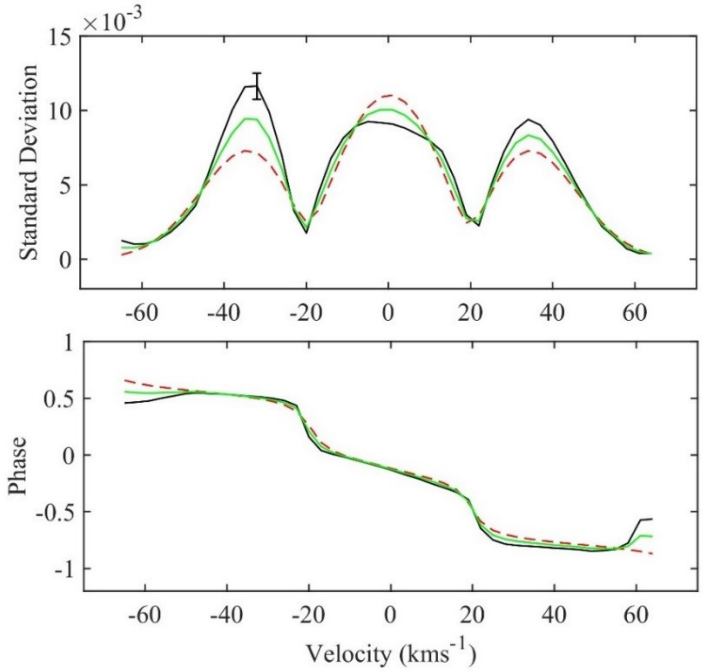

Figure 4.12: The best-fit amplitude and phase profiles for f_1 = 1.48679 d^{-1}, which is a (ℓ, m) = (1,1) mode with χ^2 = 6.7. The solid black line is the observed profile, the dashed red line is the best-fit synthetic profile, and the green represents the mean of the two. The statistical uncertainty is represented by the error bar.

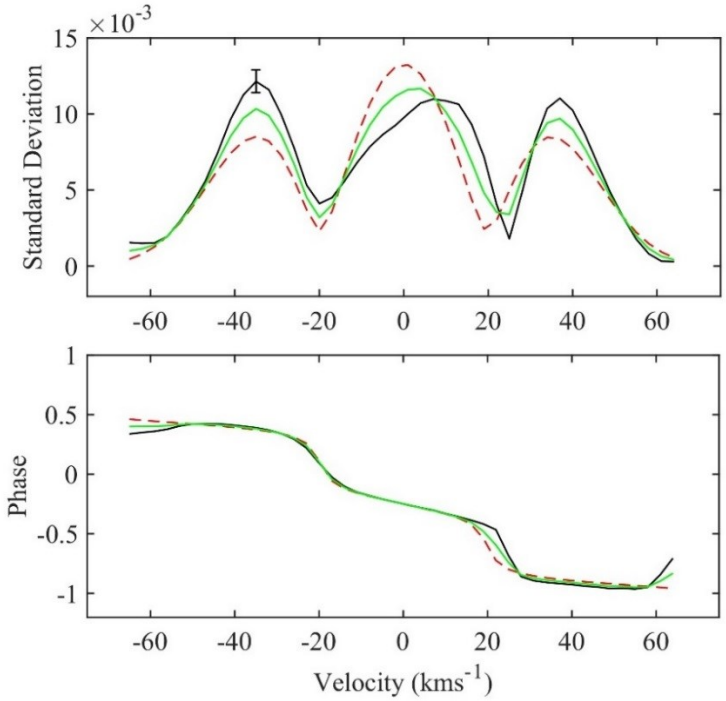

Figure 4.13: The best-fit amplitude and phase profiles for f_2 = 1.25213 d^{-1}, which is a (ℓ, m) = (1, 1) mode with χ^2 = 8.7. The solid black line is the observed profile, the dashed red line is the best-fit synthetic profile, and the green represents the mean of the two. The statistical uncertainty is represented by the error bar.

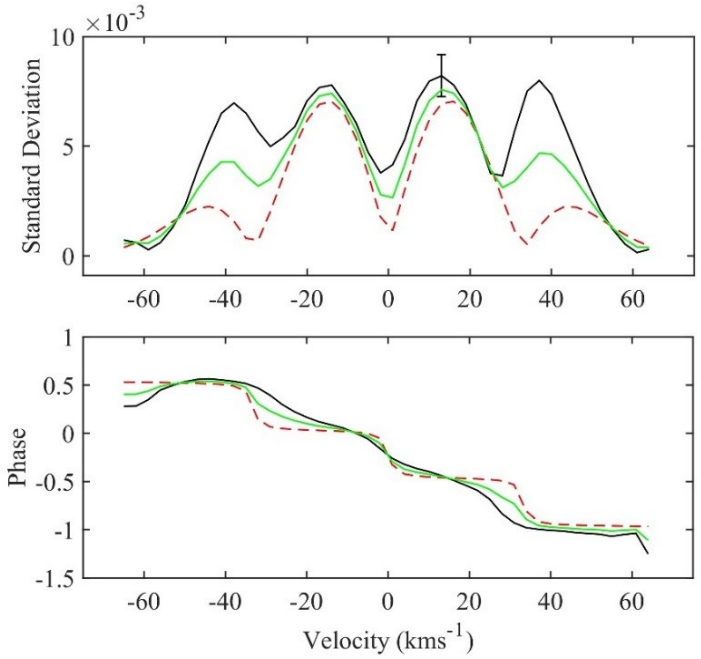

Figure 4.14: The best-fit amplitude and phase profiles for F_3 = 0.92184 d^{-1}, which is a (ℓ, m) = (3, 2) mode. The solid black line is the observed profile, the dashed red line is the best-fit synthetic profile, and the green represents the mean of the two. The statistical uncertainty is represented by the error bar.

Figure 4.11 shows the reduced χ^2 values for the models generated for each of the three frequencies. The first frequency (f_1 = 1.48679 d^{-1}) was best-fit with a reduced χ^2 value of 6.7 for an identified mode of (ℓ, m) = 1, 1 mode, while next lowest χ^2 (17.3) corresponded to a (ℓ, m) = (3, 0) mode. The standard deviation and phase fits for the best-fit mode are seen in figure 4.12. The best-fit yielded an inclination of 67.1°.

Modal analysis for the second frequency (f_2 = 1.48679 d^{-1}) yielded a best-fit χ^2 value of 9.3 for an identified mode of (ℓ, m) = 1, 1, while the next lowest χ^2 (22.92) corresponded to a mode a (ℓ, m) = (3, -2) mode. The standard deviation and phase fits for the best-fit mode are seen in figure 4.13. The best-fit yielded an inclination of 69.9°.

The final frequency (f_6 = 0.92184 d^{-1}) was best-fit with a reduced χ^2 value of 15.6 for an identified mode of (ℓ, m) = 3, 2, while the next best-fit, a (3, -2) had a reduced χ^2 of 16.2. The standard deviation and phase fits for the best-fit mode are seen in figure 4.14. The best-fit yielded an inclination of 8.9°, very close to the limit of 4.6°.

Table 4.6 lists the best-fit modes of each individual frequency with their associated χ^2 and inclinations. The modes for f_1 and f_2 agree closely with respect to mode and inclination, however the best-fit for f_6 = 0.92184 d^{-1} returned a far lower inclination and a different mode.

Table 4.6: The individual mode identifications for HD 109799.

Frequency	χ^2	Mode	Inclination (°)
f_1	6.7	1, 1	67.1
f_2	8.7	1, 1	69.9
f_6	15.6	3, 2	8.9

A simultaneous fit for all three frequencies together was then attempted, with the only varying parameters being the modes (ℓ, m), and the inclination, i. This resulted in a best combined fit with an inclination of 66.7° and a $\chi^2 = 7.9$. These best-fit results are summarised in table 4.7.

Table 4.7: Results of the combination fit for all three frequencies of HD 109799.

χ^2	f_1 (ℓ, m)	f_2 (ℓ, m)	f_6 (ℓ, m)	Inclination (°)
7.9	1, 1	1, 1	3, -1	66.7

The dominance of modes f_1 and f_2 in the combined fit is apparent. Although the three modes selected during individual fitting reappeared in combination, the result had a higher χ^2 than the final outcome, which resulted in a different mode for f_6.

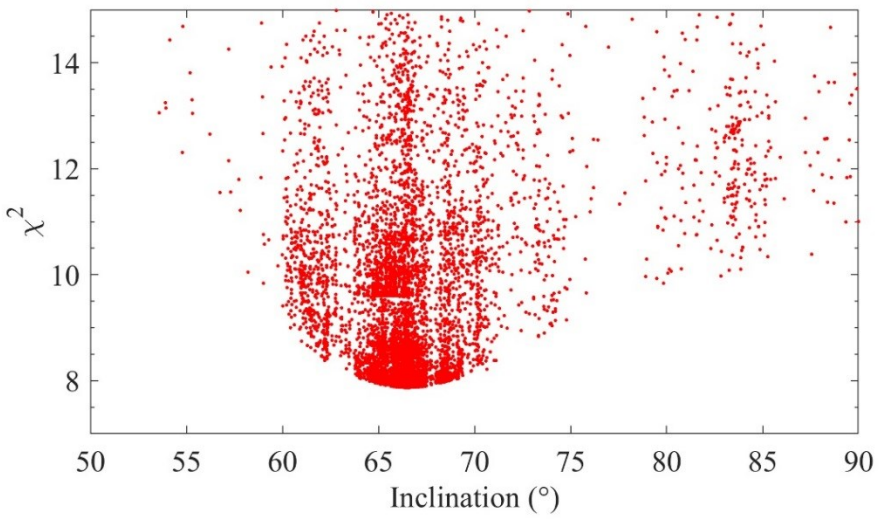

Figure 4.15: Modelled values for inclination from the combined mode fit of HD 109799, $\chi^2 = 7.8$. The inclination converged to i = 66.7°. Each red dot represents a single model.

Given FAMIAS' tendency to err towards the result with the lowest χ^2, the disparity in the outcome for f_6 compared with the individual fit is not unexpected (Brunsden, 2013). This combined fit nonetheless demonstrates excellent agreement for f_1 and f_2 reaffirming that both are genuine (ℓ, m) = (1, 1) modes. Despite the uncertainty in f_6 it is clear the inclination lies around the 65° to 70° range. Figure 4.15 shows the best-fits histogram for the modelled inclination values.

A range of values for the inclination is selected incorporating the individual best-fit inclinations for f_1 and f_2, and the combined best-fit, ranging from 65° to 70°. Using this range, and the derived $v\sin i$ (40.2 km s^{-1}), we arrive at a possible rotational velocity range for HD 109799 of v = 42.8 km s^{-1} to 44.4 km s^{-1} , significantly below the calculated Keplerian break-up limit of 501.5 km s^{-1}.

4.3 Summary

A total of 150 spectra were collected at UCMJO for the frequency and pulsation analysis of HD 109799. The addition of photometric data from HIPPARCOS introduced ambiguity to the frequency selection.

Several viable frequencies were identified in each dataset, with the two best candidates identified with confidence from the HERCULES data. These were $f_1 = 1.48679 \pm 0.00002$ d^{-1} and $f_2 = 1.25213 \pm 0.00002$ d^{-1}. A third frequency was also identified based upon its appearance in both the HIPPARCOS and HERCULES data, as well as being the sole frequency present in the literature (Handler, 1999). This frequency, $f_6 = 0.92184 \pm 0.00004$ d^{-1} was introduced with caution.

The modes identified for each frequency were $f_1(\ell, m) = (1, 1)$, $f_2(\ell, m) = (1,\ 1)$, and $f_6(\ell, m) = (3, 2)$ / (3, -1), with the latter considered to be unreliable. Nevertheless, the best-fits for the dominant frequencies, at (ℓ, m) = (1, 1), are robust. These frequencies and modes are within the typical the typical γ Doradus range of 0.3 d^{-1} to 3 d^{-1} , showing that that HD 109799 appears to be a typical γ Doradus star with variations of low harmonic degree, ℓ. Based on these results, HD 109799 can be categorised as a bona fide member of the γ Doradus class.

Since the frequencies analysed herein only account for 39.3% of the observed variation in the line-profiles, it is probably that a number of modes are yet to be discovered. Due to this, and the uncertainty in the accuracy of the frequency determination for f_6, additional observations would be welcome.

5 CONCLUSION AND FUTURE RESEARCH

Two candidate γ Doradus stars were analysed in this thesis using HERCULES spectra obtained at UCMJO: HD 103257 and HD 109799. The spectra were augmented by photometric data from the WASP archive and HIPPARCOS catalogue. The dominant frequencies detected in the spectra for each star accounted for 66% and 39.3% of the variation respectively. All the frequencies detected were in the 0.3 d^{-1} to 3 d^{-1} range typical for γ Doradus stars (Guzik, et al., 2000). The frequency identification results of HD 103257 agree with the previously published results of (Handler, 1999), lending the identifications fidelity. The modes identified in both stars are typical for the γ Doradus class and – since there were no previous mode identifications for these stars – they are the key results presented in this thesis. Based on these results, both stars are confirmed as bona fide γ Doradus stars.

Both HD 103257 and HD 109799 exhibited a dominance of (ℓ, m) = (1, 1) modes for the two highest amplitudes. This prominence may be accounted for due to the theorised lack of radial modes in γ Doradus stars, unlike δ Scuti stars, increasing the likelihood that ℓ = 1 mode is the highest-amplitude mode within the star, and bringing the star to attention as a γ Doradus candidate.

The misalignment between the synthetic and observed standard deviation profiles for HD 103257 may have arisen from distortions in the individual line profiles, either through rotational effects or through a disparity between the rotational and pulsation axis of the star. This misalignment was notably absent for HD 109799, suggesting a difficulty on the part of FAMIAS to model the unknown effect.

Given FAMIAS inability to model pulsations whose axes are offset from that of the star's rotation, it remains uncertain as to whether the pulsation axis is aligned to that of the stars' rotation for both stars. The dominance of (ℓ, m) = (1, 1) modes, however, would suggest high pulsation amplitudes, implying that the stars may be edge-on, an assertion confirmed by the inclination modelling for HD 103257.

In spite of some modelling limitations, the results within this thesis demonstrate that FAMIAS is more than capable of determining the most probable modes, as well as determining other characteristics such as inclination and radius. The applicability of FAMIAS was given further credence through its ability to model the $v\sin i$ for both stars.

The modelled value for the radius of HD 103257 ($R = 2.6R_{\odot}$) is slightly larger than that suggested by Kaye et al (1999), although since FAMIAS was designed to model δ Scuti stars, there may be a question mark on the accuracy of this figure.

The use of WASP data proved to be an invaluable asset in the verifying of frequencies found in HD 103257. HIPPARCOS photometry also proved useful, with the dominant frequencies aligning in all three datasets for this star, and the other spectroscopic frequencies reappearing as aliases and harmonics in the photometric data. Given the limited availability of high-quality photometric data for HD 109799 (only 78 HIPPARCOS data-points), the combined spectroscopy and photometry results were more ambiguous.

5.1 Future Research

Both HD 103257 and HD 109799 would be excellent targets for further analysis. A substantial amount of the variations across the line profiles for both stars remain unexplained by the frequencies found in this thesis (33.3% remain for HD 103257 and 60.7% for HD 109799). The addition of higher S/N spectra would certainly improve the quality of the least-squares fits and correspondingly, the mode identification. This may be achieved through longer exposure times and the addition of multi-site spectra to offset the effect of aliasing. This would also have the potential benefit of providing a greater alignment between spectroscopic and photometric frequency results.

The addition of spectra from space telescopes such as the Radial Velocity Spectrometer (RVS) on Gaia (Wilkinson, et al., 2005; Frémat, et al., 2017), also have the potential to provide uninterrupted long-term coverage of pulsating stars, while TESS will provide a wealth of excellent photometry (Ricker, 2014).

Based on the categorisation of HD 103257 and HD 109799 as pure γ Doradus stars, the connection between the γ Doradus and δ Scuti classes remains ambiguous. Through analysis of a greater sample of stars, a better categorisation of both types of star will surely materialise. For this purpose, the WASP archive provides a rich mine of existing data ripe for the picking.

The availability of precise stellar parameters is of great value for mode identification. The ESA satellite PLATO, planned for launch in 2024, will provide stellar radii and masses with an accuracy of 2% (Rauher, et al., 2014). Results from this mission, and other ongoing surveys, have the potential to enable more accurate frequency and mode identifications.

These observational developments would be further helped through the creation stellar models incorporating rotational effects. Factors such as granulation and turbulence – necessarily ignored in this thesis - may introduce effects within asteroseismic observations (Gray, 2005), so taking these into account during modelling provide interesting insights. Although at present the models used in FAMIAS are suitable to

describe the pulsations, ability to model any possible misalignment between the rotation and pulsation axes. Similarly, while the use of high powered cluster speeds up the modelling process immeasurably, the use of such computational resources is not available for most. As such, FAMIAS would benefit from development - particularly an increase to a 64-bit implementation.

5.2 Final Words

This thesis succeeded in determining the pulsation frequencies and modes of two γ Doradus candidates, enabling their categorisation as bona fide members of the class. Three pulsation frequencies were identified for HD 103257: 1.22496 ± 0.00001 d^{-1}, 1.14569 ± 0.00002 d^{-1} and 0.67308 ± 0.00004 d^{-1}, explaining 66.6% of the variation across the line profiles. The frequencies were characterised with best-fit modes of (ℓ, m) = (1, 1), (1, 1) and (3, -2) respectively. The inclination of the rotation axis and the radius were best-fit to i = 86.4° and R = 2.6 $R_{\odot}$, while a zero-point fit yielded a $v\sin i$ of 71.5 km s^{-1}. Three pulsation frequencies were identified for HD 109799: 1.48679 ± 0.00002 d^{-1}, 1.25213 ± 0.00002 d^{-1} and 0.92184 ± 0.00004 d^{-1} , explaining 39.3% of the variation across the line profiles. The frequencies yielded individual mode fits of modes (ℓ, m) = (1, 1), (1, 1) and (3, 2). The rotational axis for HD 109799 to the range i = 65° - 70° with a zero-point fitted $v\sin i$ of 40.2 km s^{-1}.

This thesis demonstrated the value of spectroscopic mode identifications for γ Doradus stars, as well as the value to be mined from combining data from both spectroscopy and photometry. The frequency identifications herein agreeing with those in Handler (1999) and Koen & Eyer (2002), lending further veracity to the mode identifications.

The art of asteroseismology lies in the harmony between the observational and theoretical, and the developments in both will ensure a bright future for the field. It is hoped that the results in this thesis may contribute to a deeper understanding of the beauty hidden within the stars.

APPENDIX A: RAW HERCULES FITS SPECTRA

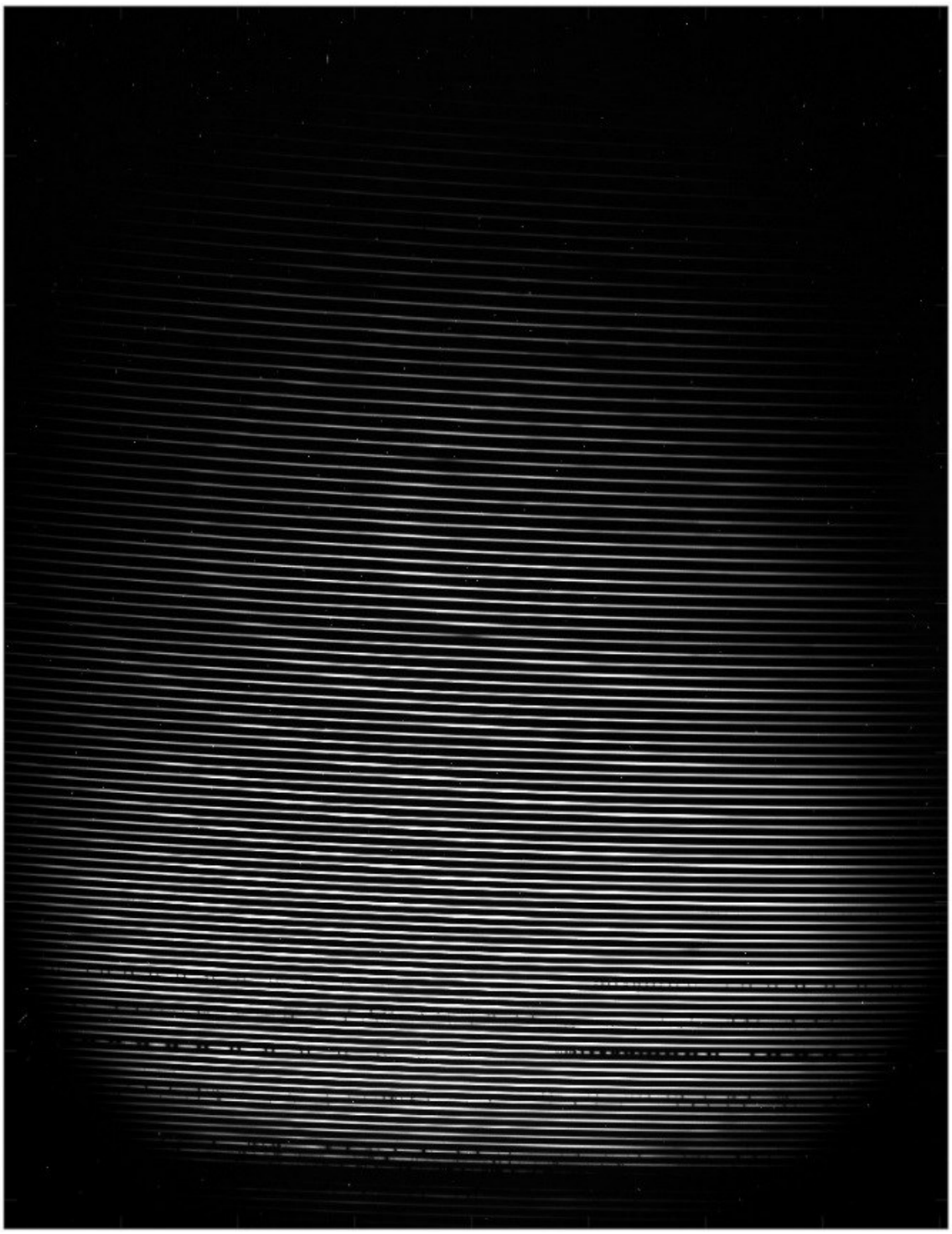

Figure A.1: A sample stellar spectrum for the star HD 103257, with the absorption lines clearly visible. The bottom of the image is the red end of the spectrum. Image taken at UCMJO in August 2016.

Figure A.2: A five second Th-Ar lamp exposure. The over exposure at the red end of the spectra is evident, and was removed in processing. The image was taken with HERCULES at UCMJO in August 2016.

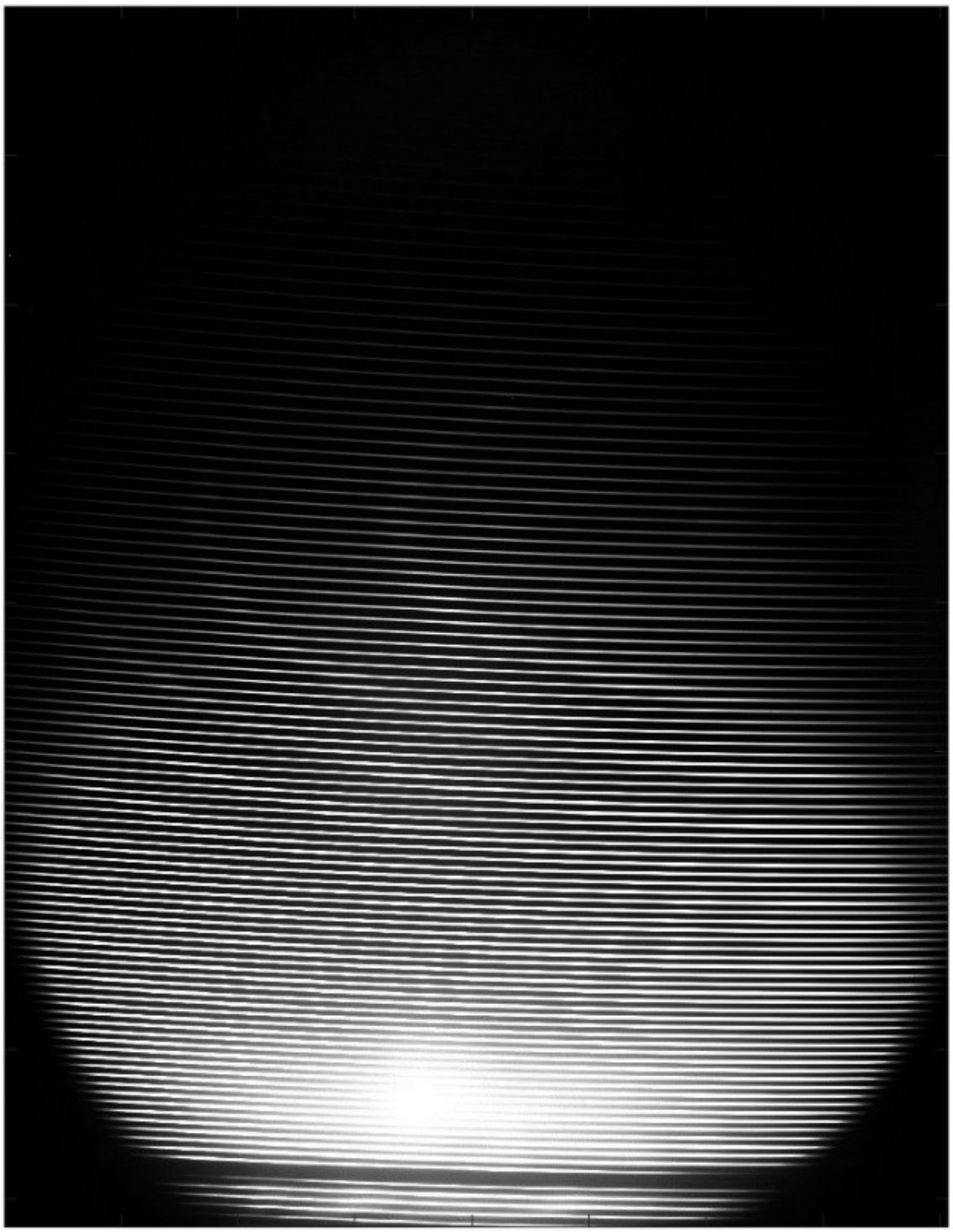

Figure A.3: An échelle spectrum for a one second flat field exposure, with characteristic lack of absorption lines. The image was taken with HERCULES at UCMJO in August 2016.

APPENDIX B: ADDITIONAL MATERIAL FOR HD 103257

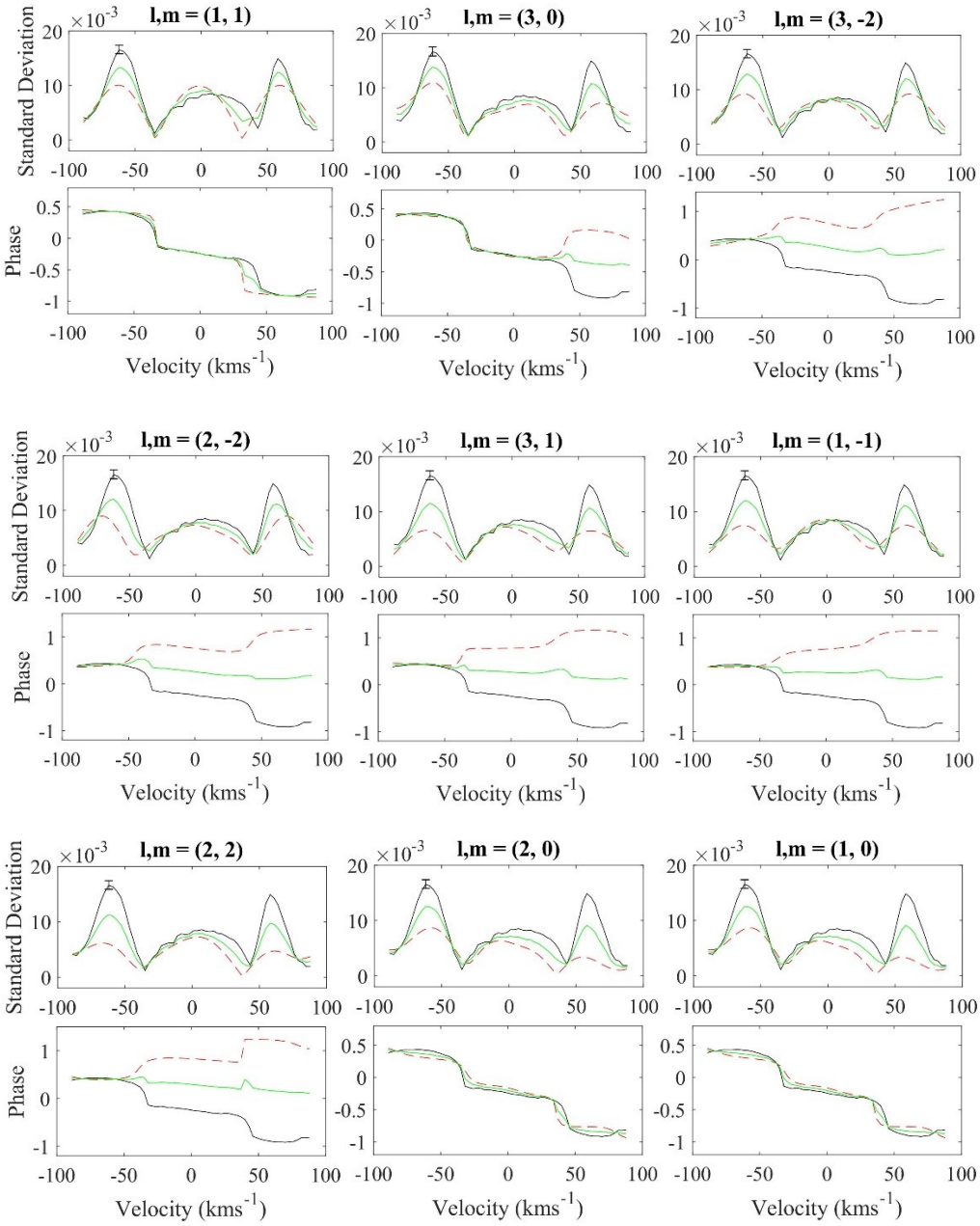

Figure B.1: An example of the best fitting procedure in FAMIAS for HD 103257. The best-fit modes for f_1 = 1.22496. The best fitting mode can be seen in the top left. The solid black line is the observed profile; the dashed red line is the synthetic profile and the green represents a mean of the two. The uncertainty is represented by the error bar.

APPENDIX C: ADDITIONAL MATERIAL FOR HD 109799

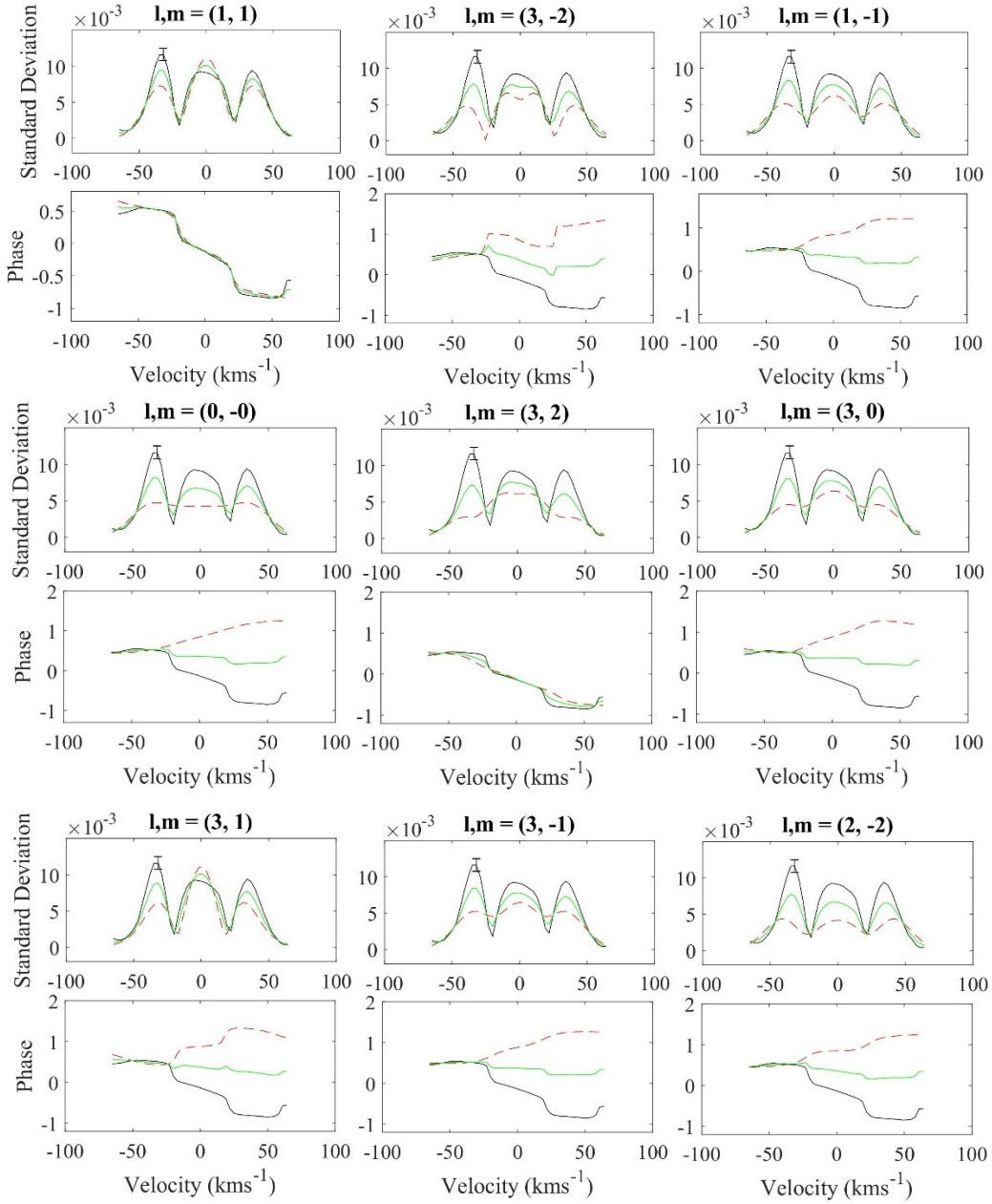

Figure C.1: An example of the best fitting procedure in FAMIAS for HD 109799. The best-fit modes for $f_1 = 1.48679$. The best fitting mode can be seen in the top left. The solid black line is the observed profile; the dashed red line is the synthetic profile and the green represents a mean of the two. The uncertainty is represented by the error bar.

REFERENCES

Aerts, C., Christensen-Dalsgaard, J., Cunha, M. & D.W., K., 2008. The Current Status of Asteroseismology. *Solar Physics,* Volume 251, p. 3.

Aerts, C., Christensen-Dalsgaard, J. & Kurtz, D., 2010. *Asteroseismology.* s.l.:Astronomy and Astrophysics Library. Springer.

Aerts, C., Eyer, L. & Kestens, E., 1998. The discovery of new gamma Doradus stars from the HIPPARCOS mission. *Astronomy and Astrophysics,* Volume 337, pp. 790-796.

Aerts, C. & Krisciunas, K., 1996. Mode identification of the slowly pulsating F0V star V398 Aurigae (9Aur). *Monthly Notices of the Royal Astronomical Society,* Volume 278, pp. 877-882.

Augustson, K. et al., 2012. CONVECTION AND DIFFERENTIAL ROTATION IN F-TYPE STARS. *The Astrophysical Journal,* 756(2), p. 23.

Baglin, A. et al., 2006. Scientific Objectives for a Minisat: CoRoT. *ESA Special Publication: Proceedings of "The CoRoT Mission Pre-Launch Status - Stellar Seismology and Planet Finding,* Volume 1306, p. 33.

Baker, N. & Kippenhahn, R., 1962. The Pulsations of Models of δ Cephei Stars. *Zeitschrift für Astrophysik,* Volume 54, p. 114.

Balona, L., 1986. Mode identification from line profile variations. *Monthly Notices of the Royal Astronomical Society,* Volume 219, pp. 111-129.

Balona, L., Daszynska-Daszkiewicz, J. & Pamyatnykh, A., 2015. Pulsation frequency distribution in δ Scuti stars. *Monthly Notices of the Royal Astronomical Society,* 452(3), pp. 3073-3084.

Borucki, W. et al., 2010. Kepler Planet-Detection Mission: Introduction and First Results. *Science,* Volume 327, pp. 977-980.

Bradley, P. et al., 2015. Results of a search for γ Dor and δ Sct stars with the Kepler spacecraft. *The Astronomical Journal,* 149(2).

Brunsden, E., 2013. *The Music of the Stars,* University of Canterbury, Christchurch, New Zealand: Doctoral Thesis.

Brunsden, E. et al., 2018. Frequency and mode identification of γ Doradus from photometric and spectroscopic observations. *Monthly Notices of the Royal Astronomical Society,* Volume 475, pp. 3813-3822.

Chapellier, E. et al., 2012. Strong interactions between g- and p-modes in the hybrid γ Doradus-δ Scuti CoRoT star ID 105733033. *Astronomy and Astrophysics,* Volume 540, p. 117.

Christensen-Dalsgaard, J., 1984. What Will Asteroseismology Teach Us. *Space Research Prospects in Stellar Activity and Variability.*

Christensen-Dalsgaard, J., 2003. *Lecture Notes on Stellar Oscillations.* s.l., Institut for Fysik og Astronomi, Aarhus Universitet.

Condon, J. & Ransom, S., 2016. *Essential Radio Astronomy.* s.l.:Princeton University Press.

Cousins, A. W. J. & Caldwell, J., 1989. The Period of gamma Doradus. *Information Bulletin on Variable Stars,* Volume 3412, p. 1.

Cousins, A. W. & Warren, P. R., 1963. *Mon. Notes Astron..* South Africa, s.n., pp. 22,65.

Cowling, T. G. & Newing, R. A., 1949. The Oscillations of a Rotating Star. *Astrophysical Journal,* Volume 149, p. 109.

Cox, J., 1980. *Theory of Stellar Pulsation.* s.l.:Prinston University Press.

Desmet, M. et al., 2009. An asteroseismic study of the β Cephei star 12 Lacertae: multi-site spectroscopic observations, mode identification and seismic modelling. *Monthly Notices of the Royal Society,* Volume 396, pp. 1460 - 1472.

Eddington, A., 1926. *The Internal Constitution of Stars.* s.l.:Cambridge University Press.

Eddington, A. S., 1917. The Pulsation theory of Cepheid variables. *The Observatory,* Volume 40, pp. 290-293.

Eyer, L. & Aerts, C., 2000. A search for new gamma Doradus stars in the Geneva photometric database. *Astronomy and Astrophysics,* Volume 398, pp. 1121-1135.

Eyer, L. & Mowlavi, N., 2008. Variable stars across the observational HR diagram. *Journal of Physics Conference Series,* 118(1), pp. 1-21.

Fracassini, L., Pastori, L., Covino, S. & Pozzi, A., 2001. Catalogue of Apparent Diameters and Absolute Radii of Stars (CADARS) - Third edition - Comments and statistics. *Astronomy and Astrophysics,* Volume 367, pp. 521-524.

Frémat, Y. et al., 2017. A Test Field for Gaia. Radial Velocity Catalogue of Stars in the South Ecliptic Pole. *Astronomy and Astrophysics,* Volume 597, p. 14.

García, R. A. et al., 2014. Rotation and Magnetism of Kepler pulsating solar-like stars. Towards asteroseismically calibrated age-rotation relations. *Astronomy and Astrophysics,* Volume 573, p. 34.

Gough, D., 1996. Asteroseismology. *The Observatory,* Volume 116, pp. 313-315.

Gray, D., 2005. *The Observation and Analysis of Stellar Photospheres.* 3 ed. s.l.:Cambridge University Press.

Grigahcène, A. et al., 2010. Hybrid γ Doradus-δ Scuti pulsators: New insights into the physics of oscillations from Kepler observations. *The Astrophysical Journal Letters,* 713(2), pp. L192-L197.

Guzik, J. A. et al., 2000. Driving the Gravity Mode Pulsations in γ Doradus Variables. *The Astrophysical Journal,* 542(1), pp. L57-L60.

Handler, G., 1999. The Domain of γ Doradus variables in the Hertzsprung-Russell diagram. *Monthly Notices of the Royal Astronomical Society,* 309(2), pp. L19-L23.

Handler, G., 2013. *Asteroseismology.* s.l.:Springer.

Hearnshaw, J. et al., 2002. The HERCULES Echelle Spectrograph at Mt. John. *Experimental Astronomy,* 13(2), pp. 59-76.

Holmberg, J., Nordstrom, B. & Anderson, J., 2007. The Geneva-Copenhagen survey of the solar neighbourhood II. New uvby calibrations and rediscussion of stellar ages, the G dwarf problem, age-metallicity diagram, and heating mechanisms of the disk. *Astronomy and Astrophysics,* 475(2), pp. 519-537.

Ibanoglu, C., Çakırlı, Ö. & Sipahi, E., 2018. The first comprehensive catalog of γ Dor pulsators and their characteristics. *New Astronomy,* Volume 62, pp. 70-84.

Kahraman-Alicavus, F. et al., 2016. Spectroscopic Survey of γ Doradus Stars I. Comprehensive atmospheric parameters and abundance analysis of γ Doradus Stars. *Monthly Notices of the Royal Astronomical Society,* 458(3), p. 393.

Kaye, A. B. et al., 1999. Gamma Doradus Stars: Defining a New Class of Pulsating Variables. *Publications of the Royal Astronomical Society of the Pacific,* 111(7), pp. 840-844.

King, J. & Schuler, S., 2005. High-Resolution Spectroscopy of Ursa Major Moving Group Stars. *Publications of the Astronomical Society of the Pacific,* Volume 117, p. 835.

Kirkby-Kent, J. et al., 2016. Absolute parameters for AI phoenicis using WASP photometry. *Astronomy and Astrophysics,* Volume 591, p. 124.

Koen, C. & Eyer, L., 2002. New periodic variables from the Hipparcos epoch photometry. *Monthly Notices of the Royal Astronomical Society,* 331(1), pp. 45-59.

Krisciunas, K., 1993. A new class of pulsating stars. *American Astronomical Society,* Issue 183, p. 1422.

Kurtz, D. W. et al., 2011. The first evidence for multiple pulsation axes: A new rapidly rotating Ap star in the Kepler field, KIC 10195926.. *Monthly Notices of the Royal Astronomical Society,* Volume 414, pp. 2550-2556.

Lomb, N., 1976. Least-squares frequency analysis of unequally spaced data. *Astrophysical Journal,* Volume 39, p. 447.

Lund, M. N., Miesch, M. S. & Christensen-Dalsgaard, J., 2014. Differential Rotation in Main-Sequence Solar-like Stars: Qualititive Inference from Asteroseismic Data. *The Astrophysical Journal,* Volume 790, p. 121.

Maisonneuve, F. et al., 2011. Frequency analysis and pulsational mode identification of two γ Doradus stars: HD 40745 and HD 189631. *Monthly Notices of the Royal Astronomical Society,* Volume 415, pp. 2977-2922.

Mantegazza, L., 2000. Mode Detection from Line-Profile Variarions. In Delta Scuti and Related Stars. *Astronomical Society of the Pacific Conference Series,* Volume 210, p. 138.

McNally, D., 1965. The distribution of angular momentum among main sequence stars. *The Observatory,* Volume 85, pp. 166-169.

Montgomery, M. & O'Donoghue, D., 1999. A derivation of the erros for least squares fitting to tme series data. *Delta Scuti Newsletter,* Volume 13, p. 28.

Moya, A., Suarez, J., Garcia Hernandez, A. & Mendoza, M., 2017. Semi-empirical seismic relations of A-F stars from COROT and Kepler legacy data. *Monthly Notices of the Royal Astronomical Society,* 471(2), pp. 2491-2497.

NASA, 2018. NASA, TESS Launch Vehicle. *NASA,* Volume tess.gsfc.nasa.gov/launch.html.

Paunzen, E. et al., 2014. HD 54272, a classical λ Bootis star and γ Doradus pulsator. *Monthly Notices of the Royal Astronomical Society,* 440(2), pp. 1020-1026.

Perryman, M. A. C. et al., 1997. The HIPPARCOS Catalogue. *Astronomy and Astrophysics,* Volume 323, pp. L49-L52.

Pesnell, W., 1987. A new driving mechanism for stellar pulsations. *The Astrophysical Journal,* Volume 314, pp. 598-604.

Pollacco, D. L. et al., 2006. The WASP Project and the SuperWASP Cameras. *The Publications of the Astronomical Society of the Pacific,* 118(848), pp. 1407 - 1418.

Pollard, K. et al., 2014. Mode identification from spectroscopy of gravity-mode pulsators. *Proceedings of the IAU Symposium,* Volume 301, pp. 477-478.

Rauher, H. et al., 2014. The PLATO 2.0 Mission. *Experimental Astronomy,* 38(1-2), pp. 249-330.

Reese, D., Lignieres, F. & Rieutford, M., 2006. Acoustic oscillations of rapidly rotating polytropic stars. II. Effects of the Coriolis and Centrifugal accelerations. *Astronomy and Astrophysics,* pp. 621-623.

Ricker, G., 2014. The Transiting Exoplanet Survey Satellite Mission. *The Journal of the American Association of Variable Star Observers,* 42(1), p. 234.

Rodriguez, E. & Breger, M., 2001. Delta Scuti and related stars: Analysis of the R00 Catalogue. *Astronomy and Astrophysics,* Volume 366, pp. 178-196.

Scargle, J., 1982. Studies in astronomical time series analysis. II - Statistical aspects of spectral analysis of unevenly spaced data. *Astrophysical Journal,* Volume 263, p. 835.

Schmid, V. & Aerts, C., 2016. Asteroseismic modelling of the two F-type hybrid pulsators KIC 100809A and KIC 10080943B. *Astronomy and Astrophysics,* Volume 592, p. 15.

Schrijvers, C. et al., 1997. Line-profile variations due to adiabatic non-radial pulsations in rotating stars. I. Observable characteristics of spheroidal modes. *Astronomy and Astrophysics Supplement Series,* Volume 121, pp. 343-368.

Skuljian, J., 2004. HRSP - A Dedicated Echelle Reduction Software Package for HERCULES. *IAU Colloquium 193: Variable Stars in the Local Group,* Volume 310, p. 575.

Smalley, B., 2013. Asteroseismology with SuperWASP. *Proceedings of the International Astronomical Union,* 9(301), pp. 39-42.

Smith, A. & WASP Consortium, 2014. Contributions of the Astronomical Observatory Skalnate Pleso. Volume 43, p. 500.

Tkachenko, A. et al., 2012. Spectrum Analysis of Bright Kepler γ Doradus Candidate Stars. *Monthly Notices of the Royal Astronomical Society,* Volume 422, pp. 2960-2968.

Townsend, R., 2003a. Asymptotic expressions for the angular dependence of low-frequency pulsation modes in rotating stars. *Monthly Notices of the Royal Astronomical Society,* Volume 340, pp. 1020-1030.

Townsend, R., 2003b. A semi-analytical formula for the light variations due to low-frequency g-modes in rotating stars. *Monthly Notices of the Royal Astronomical Society,* Volume 343, pp. 125-136.

Uytterhoeven, K. et al., 2011. The Kepler characterization of the variability among A- and F-type stars. I. General overview. *Astronomy and Astrophysics,* Volume 534, p. 125.

van Leeuwen, F., 2007. Validation of the new Hipparcos reduction. *Astronomy and Astrophysics,* 474(2), pp. 653-664.

Wilkinson, M. et al., 2005. Spectroscopic survey of the Galaxy with Gaia - II. The expected science yield from the Radial Velocity Spectrometer. *Monthly Notices of the Royal Astronomical Society,* 359(4), pp. 1306 - 1335.

Wright, D., 2008. *Spectroscopic Mode Identification in a Sample of Non-radially Pulsating Stars,* University of Canterbury, Christchurch, New Zealand: Unpublished Doctoral Thesis.

Wright, T., Egan, M., Kraemer, k. & Price, S., 2003. The Tycho-2 Spectarl Type Catalog. *The Astronomical Journal,* Volume 125, pp. 359-363.

Zboril, M., 1996. Model Atmospheres and Spectrum Synthesis; Versions of CCP7 SYNSPEC Code. *Astronomical Society of the Pacific Concerence Series,* Volume 108, pp. 193-197.

Zima, W., 2006. A new method for the spectroscopic identification of stellar non-radial pulsation models. I. The method and numerical tests. *Astronomy and Astrophysics,* 455(1), pp. 227-234.

Zima, W., 2008a. FAMIAS - A userfriendly new software tool for the mode identification of photometric and spectroscopic time series. *Communications in Asteroseismology,* Volume 157, p. 387.

Zima, W., 2008b. FAMIAS User Manual.. *Communications in Asteroseismology,* Volume 157, p. 387.